How fine is fine enough? Effect of mesh resolution on hydrodynamic simulations in coral reef environments*

Antoine Saint-Amand[a,*], Jonathan Lambrechts[b], Christopher J. Thomas[b,c], Emmanuel Hanert[a,b]

[a] *Earth and Life Institute (ELI), Université catholique de Louvain, Croix du Sud 2 bte L7.05.24, 1348, Louvain-la-Neuve, Belgium*

[b] *Institute of Mechanics, Materials and Civil Engineering (IMMC), Université catholique de Louvain, Avenue Georges Lemaître 4-6 bte L4.05.02, 1348, Louvain-la-Neuve, Belgium*

[c] *Risk Management Solutions Inc., 30 Monument Street, EC3R 8NB, London, UK*

Abstract

Coral reef environments are biodiversity hotspots that provide many services to coastal communities. They are currently facing an increasing anthropogenic pressure that jeopardises their survival. Numerical ocean models are an important tool to understand the functioning of coral ecosystems and the mechanisms ensuring their resilience. However, simulating the water circulation through reef systems is challenging because of their naturally complex topography and bathymetry. Many ocean models used for such applications have a spatial resolution coarser than the scale of individual reefs, which puts into question their suitability for the task. Here, we assess the sensitivity of a coastal ocean model's outputs to its spatial resolution when simulating the water circulation in the entire Great Barrier Reef (Australia), the largest coral reef system in the world. We consider the same model with five different resolutions near reefs, ranging from 250 m to 4 km, and compare the model outputs at different locations around reefs and in the open ocean. We also simulate the transport of passive particles released from those different locations. Our results show that the simulated tidal signal is similar for all five resolutions. However, strong discrepancies ($>$ 10 cm/s) in the current velocity are observed near the reefs and along the rugged coastline. When using a coarse-resolution model, the amplitude of the currents is overestimated over reefs, and underestimated between them. We find that validating the model at deep water mooring sites is not sufficient to ensure it performs well close to reefs. Discrepancies in currents lead to more directional and uniform tracer dispersal patterns on coarse-resolution meshes that contrast with the more dispersive patterns observed on fine-resolution meshes. Those differences at the reef level have a large cumulative effect when simulating transport processes over several weeks. Our results suggest that ocean circulation and transport simulations in coral reef environments should be based on model resolutions finer than the reef scale, which generally means a maximum resolution of about 250-500 m.

Keywords: Coastal ocean models, Spatial resolution, Coral reef environments, Dispersal patterns, Great Barrier Reef

*This is a non-peer reviewed preprint submitted to *EarthArXiv*. This preprint has recently been submitted to *Ocean Modelling* for peer review.

*Corresponding author. Email address: antoinesaintamand@gmail.com

1. Introduction

One billion people currently occupy land less than 10 m above high tide lines, of which 230 million people are below 1 m (Kulp and Strauss, 2019). These populations are directly threatened by natural hazards resulting from storms, coastal flooding and sea level rise. While huge investments are made to build coastal protection structures such as seawalls and breakwaters, they can only protect a tiny portion of the shoreline. A large part of the world's coastline therefore has to rely on natural flood defences, such as mangroves, wetlands, coral, and oyster reefs (Arkema et al., 2013). Among those, coral reefs protect about one sixth of the world's coastline, with a much larger fraction in low-income countries of the tropics. Coral reefs cover only 0.5% of the seafloor (Spalding and Grenfell, 1997) but support more than 30% of all marine species (Fisher et al., 2015). They are however degrading rapidly in response to several anthropogenic drivers, such as global warming, ocean acidification, overfishing, pollution, diseases and coastal development (Hughes et al., 2017). Between 2009 and 2018, there was a progressive loss amounting to 14% of the coral from the world's coral reefs.

Coral reefs' resilience to external disturbances strongly depends on larval exchanges between them (Underwood et al., 2009). This process, also called connectivity, can help repopulate degraded reefs by providing larvae from non-degraded reefs that can be located more than a hundred kilometres away (Bernhardt and Leslie, 2013; Green et al., 2015; Hock et al., 2017). Most coral species sexually reproduce once a year during a synchronized mass spawning event. Unlike genetic connectivity, demographic connectivity (i.e., the amount of larvae exchanged between reefs) cannot be assessed empirically and can only be estimated with biophysical models that simulate the transport of virtual coral larvae under the influence of the ocean currents. Connectivity is now a key element to inform reef conservation and restoration.

Simulating the ocean circulation in coral reef environments is particularly challenging as the bathymetry and bottom roughness can change very rapidly. These changes will drive sub-mesoscale processes at the scale at which the bathymetry and topography vary (Fringer et al., 2019). The reef geometry can for instance produce recirculation eddies, lateral flow acceleration and separation that all have a scale generally larger than the depth and of the order of the reef scale. Such processes are highly site-specific and therefore difficult to parametrize. The most reliable way to resolve flow in these areas is to explicitly increase the model resolution until it is fine enough to represent individual reefs. However, running a model with such a spatial resolution is computationally demanding, which explains why most models currently used for such applications run at a resolution coarser than the reef scale. This is for instance the case of Hock et al. (2017), Hock et al. (2019), Cheung et al. (2021) or Mumby et al. (2021) who studied connectivity to assess reef resilience in the Great Barrier Reef (GBR) with the model *eReefs* that achieves a resolution of only 4 km over coral reefs.

The impact of the hydrodynamic model resolution on the simulated circulation patterns has seldom been assessed. A few studies examined the effect of model resolution with the help of observational data, either satellite-derived data or drifter trajectories (Putman and He, 2013; Ringler et al., 2013; Colberg et al., 2020). Overall, it appears from those studies that improving the resolution reduces the model errors as compared to observations. However, this conclusion is restricted to certain specific variables or locations depending on the study. Other studies approached the issue of model resolution based on tracer dispersal to highlight possible discrepancies in hydrodynamic features (Haza et al., 2012; Zhong and Bracco, 2013; Bracco et al., 2016, 2018; Hoch et al., 2020; Pringle et al., 2021). Most of those studies highlight an improved representation of sub-mesoscales eddies at higher resolution, but only when the highest resolution tested was fine enough ($\lesssim 1$ km). Yet, impacts on horizontal velocities were not systematically observed, with differences sometimes only appearing on the vertical dispersion, or on the representation of the tidal dynamics. Finally, some studies examined the effect of model resolution on the resulting simulated connectivity for biological applications (Huret et al., 2007; Kvile et al., 2018; Dauhajre et al., 2019). While they all underline the influence of spatial resolution on simulated connectivity, those studies disagree on its effect: with some models, an increased spatial resolution led to higher local retention values, whereas a weaker and more retentive connectivity structure was observed with a coarser resolution in other cases.

Based on previous studies, no unequivocal conclusion can yet be drawn regarding the effect of model resolution on the simulated oceanographic currents. In this work, we specifically focus on hydrodynamic

simulations in coral reef environments and assess how the spatial resolution influences model outputs in such topographically-challenging systems. Instead of considering a model comparison in a geographically-limited and idealized area, we decided to run our experiments in a large-scale and realistic setting. As such, we chose to focus on the most iconic and largest corals reef ecosystem in the world, namely the GBR. The GBR presents an interesting topographical context made of thousands of shallow reefs on a very large continental shelf. Modelling the water circulation with a high resolution model in such environment is hence particularly challenging.

In this study, we use the 2D depth-integrated version of the multiscale coastal ocean model SLIM[1]. It relies on unstructured meshes and is therefore particularly well suited to coral reef environments. The resolution can be increased in intricate reef systems while remaining coarser in less complex regions. To evaluate the sensitivity of the model outputs to the spatial resolution, we tested SLIM with five different mesh resolutions. For those fives meshes, we modelled the water circulation and the transport of passive tracers throughout the domain over a period of 3 months. Using the same mathematical model formulation allowed us to keep the physics unchanged and to focus only on the numerical model resolution.

2. Material and methods

2.1. Study area

The GBR extends along the northeastern coast of Australia over 2000 km in length and up to 200 km in width. It is the largest coral reefs assemblage in the world, composed of more than 3000 individual reefs. Those reefs, all located on the continental shelf, are found in very different shapes and sizes, ranging from 0.01 km^2 to 100 km^2. In some regions, especially in the North, the reef matrix is very dense, occupying up to 90 % of the along-shelf length. Other regions exhibit a more scattered structure, representing no more than 10 % of the along-shelf length (Wolanski et al., 2003). Most of the reefs lie a few meters below the sea surface. The bathymetry of the sea bed surrounding the reefs remains relatively shallow on the whole continental shelf, with about 50-100 m depth (Fig. 1).

The ocean circulation in the GBR is driven by wind, tides and the large-scale circulation from the Pacific Ocean (Pickard et al., 1977; Wolanski, 1983; Wolanski and Pickard, 1985; Brinkman et al., 2002; Wolanski et al., 2003; Lambrechts et al., 2008). The resulting ocean currents are strongly impacted by the complex topography of the GBR with reefs acting as barriers to the water flow. Tidal currents have a major effect on the water circulation, and particularly dominate cross-shelf processes (Andrews and Bode, 1988). Those tidal currents usually dictate the flow over timescales of hours, with tidal spectra dominated by diurnal and semi-diurnal constituents (Wolanski, 1983). On the other hand, the wind-driven circulation and the large-scale exchanges with the Coral Sea prevail over longer timescales.

The large-scale circulation in the region is governed by the South-Equatorial Current (SEC) coming from the Southwest Pacific Ocean and flowing Westward towards the Australian coast. When entering the Coral Sea, the SEC hits the islands of Vanuatu and New Caledonia, and splits into three distinct jets (Fig. 1): the North Vanuatu Jet (NVJ), the North Caledonia Jet (NCJ), and the South Caledonia Jet (SCJ) (Brinkman et al., 2002; Kessler and Cravatte, 2013; Ganachaud et al., 2014; Colberg et al., 2020). Those three jets drive the main intrusion of water form the Coral Sea in the GBR. More specifically, the NVJ and the NCJ play the major role as they both reach the GBR in its central part, where the reef matrix is more scarce and therefore more permeable to external water inflow (Thomas, 2015).

In the North, the NVJ is a shallow current limited to the upper ocean. When approaching the Australian coast, the NVJ splits in two: the largest part turns North and form the North Queensland current (NQC) which inducts in turn the Papua Gyre (PG) and the Gulf of Papua Current (GPC), whereas a smaller part turns South to initiate the East Australian Current (EAC). The point of bifurcation of the NVJ is known to vary seasonally and inter-annually (Wolanski et al., 2003) and to oscillate between latitudes 14°S-20°S (Brinkman et al., 2002). Further South, the deeper NCJ (extending at least to 1500 m depth), approaches

[1]Second-generation Louvain-la-Neuve Ice-Ocean Model. See `https://www.slim-ocean.be` for more details about the model. This model is open-source and publicly available here: `http://git.immc.ucl.ac.be/slim/slim`.

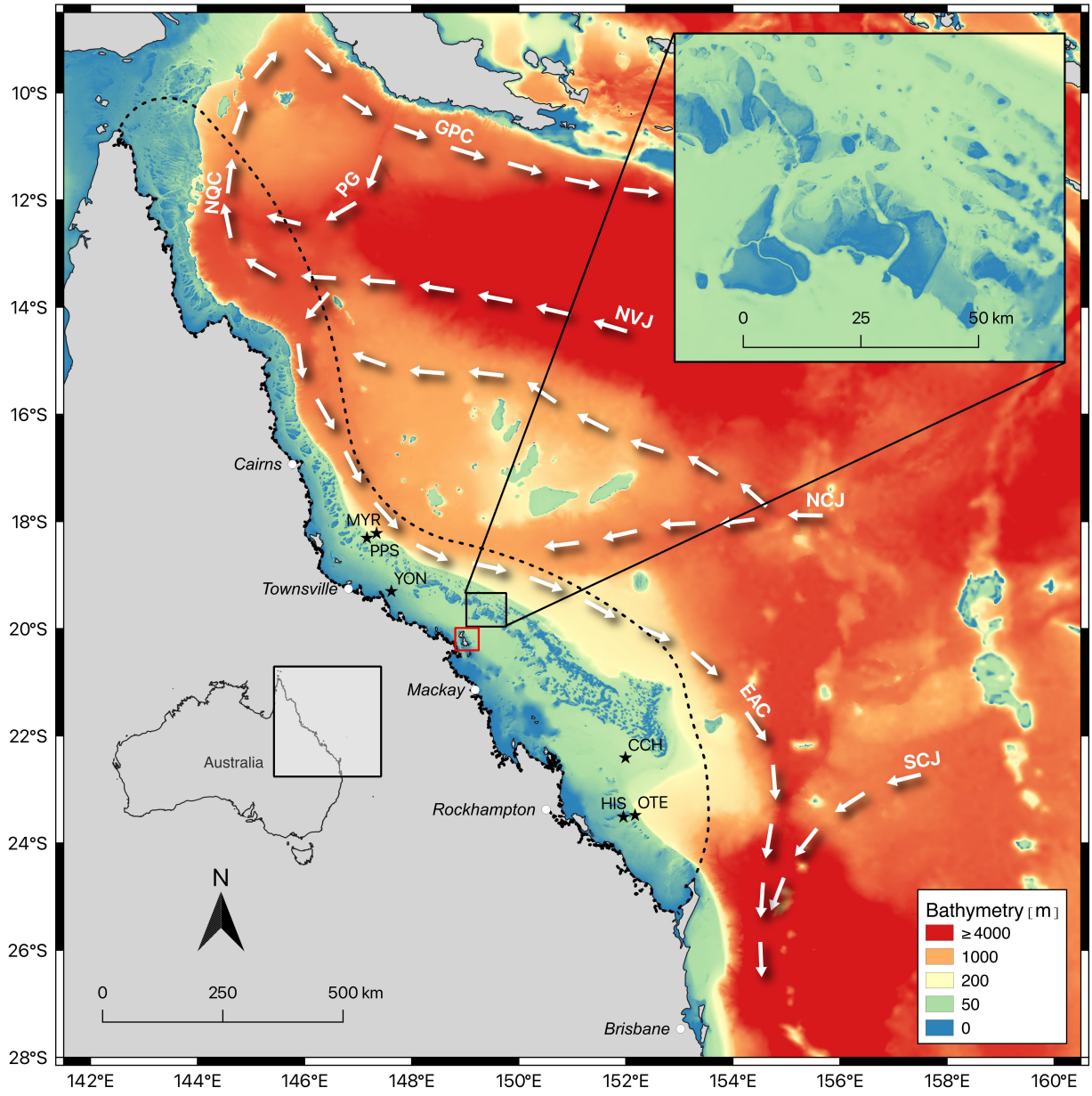

Figure 1: Model's area of interest (dashed line), bathymetry and main large-scale ocean currents (white arrows). The close-up view highlights the complex bathymetry within the reef system. It also shows deeper narrow passages between the reefs. The mooring stations are indicated with black stars. The red square indicates the extent of the area shown in Fig. 3.

the Coral Sea at a latitude of 18°S. It splits into two branches around the Queensland Plateau before merging again to flow mostly Northward underneath the EAC, and eventually joining the NQC. Finally, the SCJ reaches the shore at the extreme South of the GBR where it turns southward to merge into the EAC.

2.2. Hydrodynamics

With its succession of shallow reefs and deeper regions between them, the topography of the GBR is particularly intricate, causing the water circulation to be in turn very complex. It is therefore important to use an ocean model able to represent both small- and large-scale flow features. In this study, we use the 2D barotropic unstructured-mesh ocean model SLIM (Lambrechts et al., 2008). SLIM has already been applied multiple times to the GBR for connectivity, sediment transport and plastic pollution studies (e.g., Lambrechts et al., 2010; Thomas et al., 2014, 2015; Critchell et al., 2015; Grech et al., 2016; Schlaefer et al., 2022; Saint-Amand et al., 2022).

SLIM simulates the sea surface elevation η and the depth-averaged current velocity $\boldsymbol{u}$ by solving the non-linear shallow water equations:

$$\frac{\partial \eta}{\partial t} + \boldsymbol{\nabla} \cdot (H\boldsymbol{u}) = 0, \tag{1}$$

$$\frac{\partial \boldsymbol{u}}{\partial t} + \boldsymbol{u} \cdot \boldsymbol{\nabla}\boldsymbol{u} + f\boldsymbol{e}_z \times \boldsymbol{u} = -g\boldsymbol{\nabla}\eta + \frac{\boldsymbol{\tau}}{\rho H} + \mathbf{D}, \tag{2}$$

where $H = h+\eta$ is the water column height, h is the bathymetry (in order to ensure that the entire domain is under water during the whole simulation, the minimum depth is set to $h = 5m$), f is the Coriolis parameter, $\boldsymbol{e}_z$ is a unit vector pointing vertically upwards, g is the gravitational acceleration. The penultimate term in Eq. 2 accounts for the effect of wind on water motion and follows the parametrization described in Smith and Banke (1975). In this term, $\boldsymbol{\tau}$ represents the surface wind stress and ρ is the water density. The wind velocity is computed by the model ACCESS[2] and made available through eReefs datasets[3]. Finally, $\mathbf{D}$ includes the momentum dissipation terms, and is expressed as follows:

$$\mathbf{D} = \frac{1}{H}\boldsymbol{\nabla} \cdot [H\nu(\boldsymbol{\nabla}\boldsymbol{u})] - \frac{C_d||\boldsymbol{u}||\boldsymbol{u}}{H}. \tag{3}$$

The first term is the momentum diffusion with a Smagorinsky (1963) non-linear viscosity ν. The second term accounts for the bottom friction. The bulk drag coefficient C_d was set to 2.5×10^{-3} and multiplied by 20 over reefs to account for the increased roughness of the reef surface (Monismith, 2007).

On the open boundaries, the exchanges with the Coral Sea are included in the model by forcing it with the sea surface elevation and velocity fields from the global ocean circulation model NEMO[4] (Madec et al., 2019). Daily outputs are available through CMEMS[5] on a regular grid with a horizontal resolution of $1/12°$ and 50 vertical layers. A tidal signal, constructed from TPXO9.v3 (Egbert and Erofeeva, 2002), was also imposed on the open boundaries. Eqs. 1 and 2 were solved from December 1, 2020 to March 1, 2021, with a spin-up period of 2 days. The time integration scheme is 2nd-order implicit, and the time step is set to 15 min.

2.3. Mesh generation

We built five different meshes where we varied the maximum spatial resolution. Those unstructured meshes were generated by following the method outlined in Legrand et al. (2006) and were computed thanks to the Seamsh python library[6] wrapping the open-source mesh generator GMSH (Geuzaine and Remacle, 2009). The mesh resolution depends on the bathymetry (such that the resolution is proportional to gravity

[2]Model developed by the Bureau of Meteorology (`http://www.bom.gov.au/nwp/doc/access/NWPData.shtml`)
[3]For more details on eReefs, see `https://research.csiro.au/ereefs/`
[4]Nucleus for European Modelling of the Ocean, `http://www.nemo-ocean.eu`
[5]Copernicus Marine Service, `https://marine.copernicus.eu`
[6]See repository here: `https://git.immc.ucl.ac.be/jlambrechts/seamsh`

waves speed) and on the distance to the coastlines, to the reefs and to the 200 m isobath. The target element size is then defined as:

$$r(\boldsymbol{x}) = r_{\min} + \phi(d(\boldsymbol{x}))\sqrt{\frac{h(\boldsymbol{x})}{h_{\max}}}(r_{\max} - r_{\min}), \tag{4}$$

where $d(\boldsymbol{x})$ is the minimum between the distance to the nearest reef, to the nearest coast, and to the shelf break at position $\boldsymbol{x}$, $r_{\min}$ and $r_{\max}$ are respectively the minimum and maximum prescribed element size (the latter being set to 25 km for all the meshes used in this study), and $h_{\max}$ is the upper threshold on depth, set here to 500 m ($0 \leq h(\boldsymbol{x}) \leq h_{\max}$). This means that the mesh size is unaffected by bathymetry changes over this limit. The bathymetry used for the mesh generation is coming from Beaman (2010). This dataset has a spatial resolution of 100 m. The coastlines and the reef map are both provided by the Great Barrier Reef Marine Park Authority (Lawrey and Stewart, 2016).

The function $\phi(d)$ is a blending function that ensures a smooth transition between fine and coarse resolution regions. In this work, we used a basic linear function ensuring a smooth transition between both regions:

$$\phi(d) = \begin{cases} 0 & 0 \leq d \leq d_0 \\ \dfrac{d - d_0}{d_1 - d_0} & d_0 \leq d \leq d_1 \\ 1 & d_1 \leq d \end{cases} \tag{5}$$

where d_0 is the length of the plateau along reefs and islands where resolution is the finest. We chose to match this value to the minimum element size (so that $d_0 = r_{\min}$). In other words, the length of the plateau is always equal to exactly one element. On the other side, d_1 denotes the length of the transition zone (plateau included) between regions with minimal and maximal resolution. The value of that parameter was kept to a constant value $d_1 = 100$ km for all meshes.

The finest resolution of the meshes generated for this work was doubled between each mesh. We hence consider 5 different meshes with minimal resolutions $r_{\min}$ of 250 m, 500 m, 1 km, 2 km and 4 km respectively.

2.4. Model evaluation

The quality of each model setup and the differences between them are first assessed by comparing the simulated velocity and sea surface elevation with measurements from the IMOS (2018) mooring stations (Fig. 1). This network historically contained ten stations, but some are now fully decommissioned, and some others did not operate during the period considered in this study. We therefore had to restrict our analysis to the six stations that were operational during our simulation period. Three of those stations are located in the Central GBR, while the three others are in the extreme South of the GBR (see black stars in Fig. 1). For each mooring station, velocities are given at several depth levels, and were thus depth-averaged in order to make them comparable with our 2D model outputs. For every station, we also subtracted the three-months mean value from every sea surface elevation entry to derive the sea surface anomalies over the simulation period.

In order to assess the impact of mesh resolution on the model accuracy in coral reef environments, we randomly selected 300 points throughout the GBR as follows: 1/3 over the reefs, 1/3 within a 1 km buffer zones around the reefs, and 1/3 further than 5 km away from the closest reef and coastline (Fig. 2). None of those points were taken in areas deeper than 200 m to focus on the shallow GBR environment and not on the deeper ocean. At each point, we extracted the time-series of modelled sea surface elevations, current amplitudes and current directions for the five model setups. The 500 m, 1 km, 2 km and 4 km model results were compared to the 250 m model taken as a reference. The sea surface elevation, current direction, and current amplitude were assessed by computing the mean absolute errors (MAE) and the bias. The differences of sea surface elevation were computed on hourly data to take the tidal signal into account. Conversely, we compared currents amplitude and direction on daily averaged data to focus on the residual currents.

We also conducted a tidal analysis with the python reimplementation of the Utide package (Codiga, 2011). We extracted the main tidal constituents from the velocity time series at the 300 random points

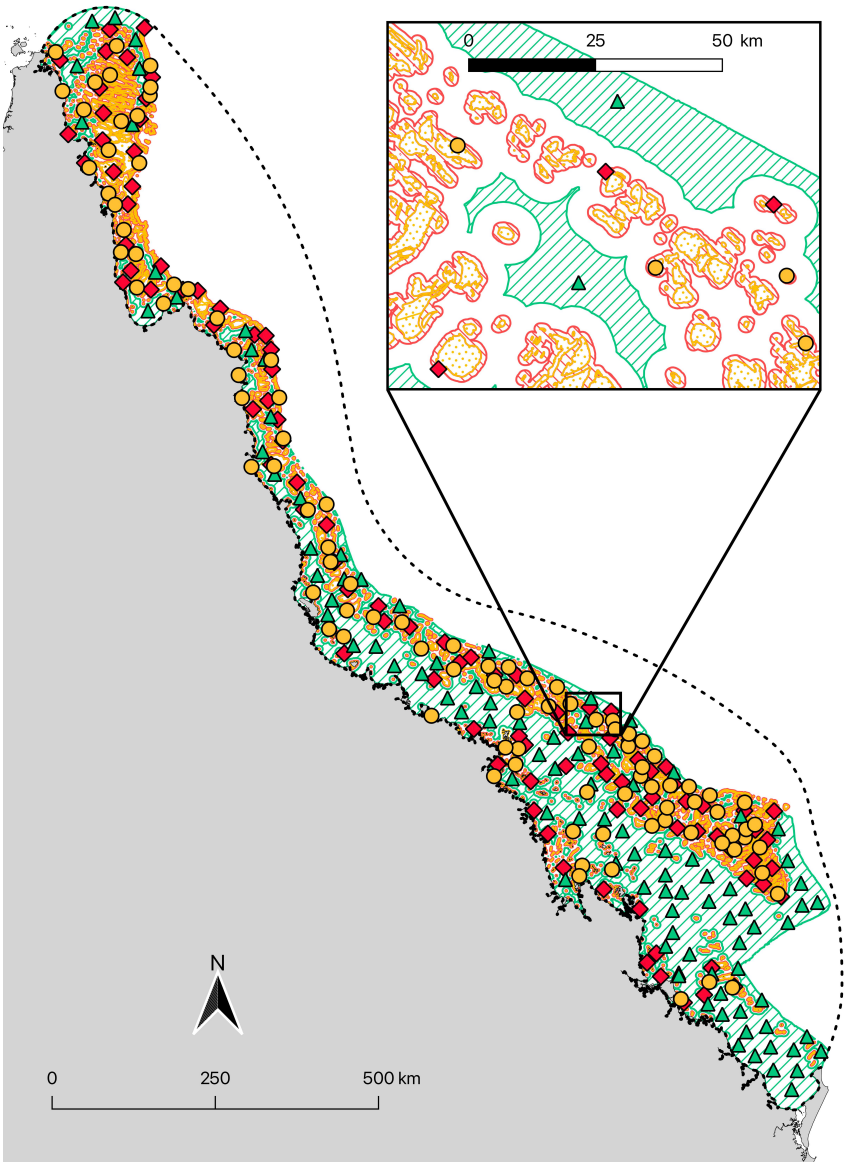

Figure 2: Randomly selected locations where models with different mesh resolutions are compared. The yellow circles are located over the reefs (within the orange dotted areas), red squares are located between 0 and 1 km from reefs (within the pink hatched areas) and green triangles are located at more than 5 km away from reefs (within the light green hatched areas). No points are located in zones deeper than 200 m. The extent of the model domain is shown with a dashed line.

described before. Each constituent is described by its amplitude, phase lag, and percent energy (PE). This last metric represents the relative importance of each constituent based on the kinetic energy they encompass (Codiga, 2011). We compared the different model setups by computing the mean of absolute differences in PE constituent-wise between the reference 250 m setup and the four other setups. For the clarity of the analysis, we only consider the five dominant (semi-)diurnal constituents, namely M2, S2, K1, N2, O1.

We finally assessed the cumulative impact of mesh resolution on the hydrodynamics by simulating the transport of 2000 passive particles released from each of the 300 points mentioned before (Fig. 2). The stability of the results has been tested by conducting the same analysis with twice as many particles (i.e., 4000 particles released at each point). We started the transport simulations on October, 1 2018, and then tracked the particles for three months with a time step of 200 s. We considered different metrics characterizing the particles dispersal patterns to assess the differences between the five model setups according to the particles release locations. Those metrics are calculated for the 3 main release areas (i.e., over reefs, within 1 km of a reef or more than 5 km away) that contain each 100 release points. They all rely on the centroids of the cloud of particles released from location i ($i = 1, \ldots, 100$), given by:

$$\overline{\mathbf{x}}_i(t) = \frac{1}{n_i(t)} \sum_{j=1}^{n_i(t)} \mathbf{x}_{i,j}(t) = (\overline{x}_i(t), \overline{y}_i(t)) \tag{6}$$

where $\mathbf{x}_{i,j}$ is the position of particle j released from location i at time t ($j = 1, \ldots, n_i(t)$), and $n_i(t)$ is the number of particles released from location i floating in the domain at time t.

The mean dispersal distance, the spread, and the offset between clouds of particles have been computed thanks to the following three metrics:

- The mean distance $DR(t)$ from the release location is computed by averaging the Euclidean distance between the release location and the centroid of the cloud of particles released from that location:

$$DR(t) = \frac{\sum_{i=1}^{100} ||\overline{\mathbf{x}}_i(t) - \mathbf{c}_i||}{100} \tag{7}$$

  where $\mathbf{c}_i$ represents the coordinates of the release location i. This metric describes how far particles travel from their release location.

- Given the geometry of the domain, an anisotropic dispersion is expected. The dispersion of particles is hence computed in both the major and perpendicular directions (denoted ξ and η, respectively) following the approach developed in Rypina et al. (2012) and Petton et al. (2020). Those dispersions are obtained from the components of the single-particle dispersion tensor:

$$D_{xx,i}(t) = \frac{1}{n_i(t)} \sum_{j=1}^{n_i(t)} |x_{i,j}(t) - \overline{x}_i(t)|^2 \tag{8}$$

$$D_{yy,i}(t) = \frac{1}{n_i(t)} \sum_{j=1}^{n_i(t)} |y_{i,j}(t) - \overline{y}_i(t)|^2 \tag{9}$$

$$D_{xy,i}(t) = \frac{1}{n_i(t)} \sum_{j=1}^{n_i(t)} |x_{i,j}(t) - \overline{x}_i(t)| \, |y_{i,j} - \overline{y}_i(t)| \tag{10}$$

  The dispersions in the major and perpendicular direction hence read:

$$D_\xi(t) = \frac{1}{100}\sum_{i=1}^{100}\left(D_{xx,i}(t)\cos^2(\theta_i(t)) + D_{yy,i}(t)\sin^2(\theta_i(t)) + D_{xy,i}(t)\sin(2\theta_i(t))\right) \tag{11}$$

$$D_\eta(t) = \frac{1}{100}\sum_{i=1}^{100}\left(D_{xx,i}(t)\sin^2(\theta_i(t)) + D_{yy,i}(t)\cos^2(\theta_i(t)) - D_{xy,i}(t)\sin(2\theta_i(t))\right) \tag{12}$$

where θ is the rotation angle between the zonal direction and the direction of the fastest spread (Rypina et al., 2012). This angle is estimated by maximizing $D_\xi(t)$:

$$\tan(\theta_i(t)) = \frac{D_{yy,i}(t) - D_{xx,i}(t) + \sqrt{(D_{yy,i}(t) - D_{xx,i}(t))^2 + 4D_{xy,i}(t)}}{2D_{xy,i}(t)} \tag{13}$$

- The offset between clouds of particles transported by currents computed on different meshes is represented by the average distance $DC_k(t)$ between the centroids on the 250 m mesh and the corresponding centroids on any other mesh:

$$DC_k(t) = \frac{\sum_{i=1}^{100} ||\overline{\mathbf{x}}_{i,k}(t) - \overline{\mathbf{x}}_{i,250}(t)||}{100} \tag{14}$$

where $\overline{x}_{i,k}(t)$ represents the position of the centroid of particles released from point i on mesh k, and $\overline{x}_{i,250}(t)$ the position of the centroid of particles released from point i on the 250 m mesh, taken as the reference.

3. Results

The number of elements included in the mesh roughly triples each time we increase the highest resolution by a factor of two (Tab. 1). The number of elements composing the finest mesh ($\sim 3.3 \times 10^6$) is therefore approximately 100 times larger than for the coarsest. In all meshes, the coarsest elements have almost the same size of about 28 km, which is slightly larger than the target maximum size of 25 km. Conversely, as one can expect, differences between meshes appear strongly in terms of mean and minimum element size. The average edge lengths are indeed not much greater than the intended highest resolution, and minimum edge lengths are even below those threshold values. Topographical constraints can sometimes force the mesh generator to use elements smaller than the target element size in order to preserve smooth changes in the mesh resolution. When sorting all the elements composing meshes by size from the smallest to the largest, the smallest 50% mesh elements covers nearly 30% of the entire domain in the coarsest mesh. This fraction drops to less than 15% on the finest mesh, showing that the increased level of details is focused on targeted regions. On the finest mesh the smallest 99% mesh elements cover only a bit more than 50% of then entire domain surface area, while for the coarsest mesh this fraction reaches ∼85%.

The hydrodynamics being strongly forced by the topography and bathymetry, it is important to represent them as accurately as possible. This is achieved in a cost-effective manner by locally increasing the mesh resolution along the coastline and over coral reefs. Here, the mesh that locally reaches the highest resolution of 250 m is composed of 3.3×10^6 elements. A uniform mesh with the same resolution over all the domain would have about five times more elements. Fig. 3 shows snapshots of all meshes with a focus on the exact same region of the Whitsunday Islands (corresponding to the red square in Fig. 1). When moving from a 250 m to a 4 km mesh, there is a clear loss of topographical details. More importantly, when using the coarsest 4 km mesh, all the islands of the Whitsundays are merged together and connected to the mainland, hence totally blocking the circulation. On the other hand, we can distinguish nearly all the small islands composing the Whitsundays when using the 250 m mesh. When comparing the currents simulated on a 4 km and on a 250 m mesh, it clearly appears that mesh resolution can strongly impact the circulation patterns (Fig. 4). In addition to providing more fine-scale details of the circulation, such as flow meandering

Table 1: Specifications of the five meshes, from the coarsest to the finest. The size section of the table depict the minimum, mean, and maximum of the average element size, in km.

	Finest resolution	**4 km**	**2 km**	**1 km**	**0.5 km**	**0.25 km**
	Nb. of elements	3.97×10^4	1.28×10^5	3.97×10^5	1.17×10^6	3.28×10^6
Size	Minimum	1.99	0.87	0.41	0.19	0.10
	Mean	4.60	2.43	1.29	0.69	0.38
	Maximum	27.99	27.07	29.04	28.68	26.96

and recirculation eddies, local mesh refinements can also impact the larger scale circulation patterns along coastlines. In this illustration over the Whitsundays, the use of a 4 km mesh totally prevents the circulation between the mainland and the islands, which leads to a reversal of the flow direction in all the western part of this area. This obviously has important consequences for transport processes in that area such as coral larvae dispersal. Further offshore, east and north of the islands, the circulation patterns are generally comparable in both cases, except for weak currents at tidal reversal (like on Fig. 4). The large scale circulation hence does not seem to be affected by local changes in mesh resolution.

When comparing the sea surface elevation and the currents at the 3×100 random points, two main trends appear. Firstly, for the three different environments, the average differences for all variables linearly increase as the mesh becomes finer (Fig. 5). Moreover, the currents velocity is more impacted by the mesh resolution over and near coral reefs. Indeed, the differences in current amplitude and direction appear to be around three times larger for points over or near the reefs than for those further away (Fig. 5). For those last points, it is worth noting that some differences are still observed between meshes, probably related to a better reproduction of the topography and bathymetry on finer meshes. The order of magnitude of differences regarding sea surface elevation seems to be comparable whatever the distance to reefs, even if slightly larger for on and near reef points (Fig. 5). Just as with the validation data from mooring stations, we can again observe that the effect of mesh resolution on the sea surface elevation signal, while non-negligible, is quite limited (MAE of 6 cm between the finest and coarsest mesh compared to a tidal range of $\sim$3 m). Besides, the effect of mesh resolution on this variable is roughly homogeneous throughout the domain.

Compared to the MAE, the biases between the model outputs on the 250 m mesh and any other mesh are very limited for both sea surface elevation and current direction. No trend between meshes emerges for those two variables. On the other hand, the bias for the current amplitude displays contrasting trends between sampling locations: the bias is negligible for currents far from the reefs, it is always positive over the reefs, and always negative in the vicinity of reefs. The magnitude of this bias increases as the mesh becomes coarser. This diverging trend can be explained by the discretization of coral reefs and their larger friction on the different meshes. On coarser meshes, the resolution is often larger than the reef size and mesh elements usually overstep the reefs. Since the bottom drag is computed on the element nodes and then linearly interpolated between them, large mesh elements over coral reefs will generally have a bottom drag that is lower that the drag of coral reefs and larger than the drag of a sandy seabed. As a result, the current velocity will be over-estimated over the reefs and under-estimated in the vicinity of reefs. In other words, with a coarse-resolution mesh, the friction associated with coral reefs is spread over an area larger than the reef itself.

The main tidal constituents contain on average the same fraction of the total tidal energy for the three types of environment (on reef, near reef and open-sea points, Fig. 6). As already seen with the MAE computed on the currents (Fig. 5), differences increase as the resolution becomes coarser. However, the average differences between the results from the finest mesh and from the coarser meshes is not comparable between the three types of environment. Constituent-wise, differences at random points located over or in the direct vicinity of coral reefs appear to be roughly twice as large as in the open sea. It is also interesting to note that, even if they represent a tiny fraction of the percent energy in the full tidal signal, diurnal constituents (K1 and O1) display proportionally greater relative differences between meshes than

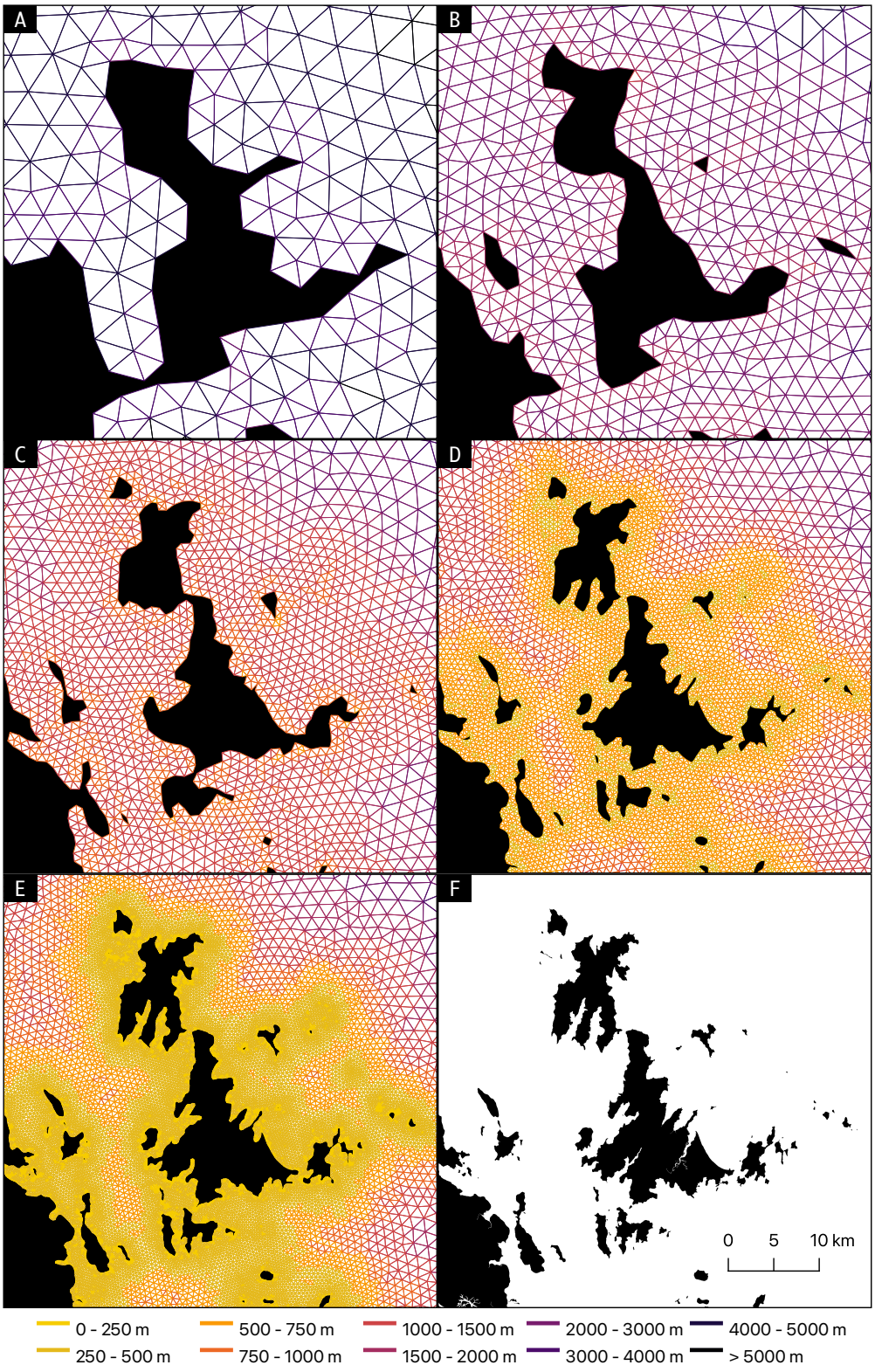

Figure 3: Comparison of the five meshes of increasing resolution over the Whitsunday Islands (red square in Fig. 1). A to E: meshes with finest resolution of 4000, 2000, 1000, 500 and 250 m. Mesh elements are coloured by their maximum edge length. F: Mainland and islands as they appear in the original topography. On the 4000 m setup, all the Withsundays islands are merged together and connected to the mainland, whereas the finest setup allows for most of the islands to appear on the mesh.

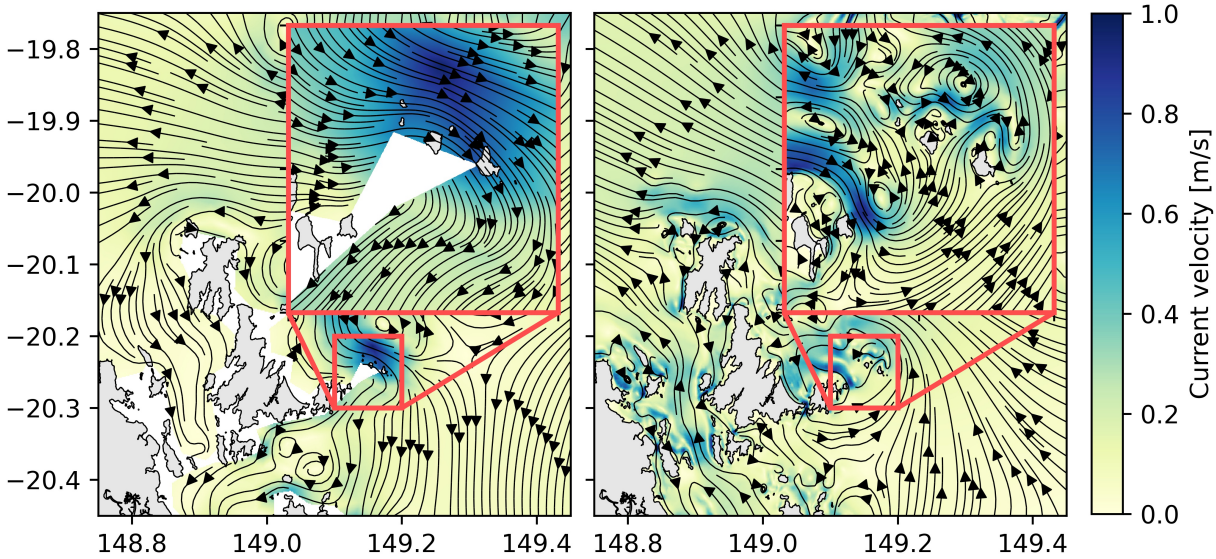

Figure 4: Snapshot of simulated currents in the Whitsundays' area on the coarsest (left) and finest (right) meshes on the 15th of December 2020 8:00 am (UTC time). The colour background represents the current amplitude in m/s, with streamlines on top. Mainlands and islands are displayed in grey. White areas are not taken into account by the mesh due to lack of resolution. The large-scale circulation patterns are similar, but the inset highlights strong differences regarding small-scale features caused by reefs and islands.

semi-diurnal constituents (M2, S2 and N2).

We also estimate the cumulative effect of the mesh resolution on the simulated ocean currents by studying the dispersal of clouds of passive particles released from the three different environments (Fig. 7). The mean distance separating particle clouds from their release location exhibits a similar trend on all meshes whatever the release location. In all cases, it increases in an almost linear fashion, and reaches slightly higher values for particles released far from the reefs.

Differences between the five meshes appear more clearly when looking at the spread of the particle clouds around their centroids as measured by the dispersions in the major and perpendicular axes. Clouds of particles released over or close to the reefs tend to spread more in both directions, and hence cover a larger surface area, when currents are simulated on a fine mesh. The spread of the clouds can be as much as twice larger on the finest mesh than on the coarsest one. Conversely, clouds of particles released in the open sea display dispersions that are much more similar for all five meshes. From the comparison between average dispersions in the major and perpendicular directions, we highlight a significant anisotropy in the spread of particles: whatever the mesh and the release environment, the dispersion in the major direction is twice to five times higher than the dispersion in the perpendicular direction. The average angle of major dispersion is nearly constant during the whole simulation and is oriented parallel to the coast whatever the mesh and release location.

Comparing the positions of particle cloud centroids between the 250 m mesh and the other coarser meshes reveals that the average distance between the cloud centroids can reach about 50 km for the coarsest mesh. The distance almost reaches ∼20 km for a 500 m mesh resolution, hence highlighting the important cumulative effect of the hydrodynamic model resolution on the transport processes. Results for particles released on and near reefs display very similar distances, while clouds of particles released far from the reefs show slightly smaller differences. The differences between particle cloud spread curves tend to stabilize after about a month. This suggests that most of the differences are induced by the first days of simulation when particles are the closest to the reefs, i.e., where velocity fields simulated on the five meshes are most different. Particles tend to stay a longer close to their release point on finer meshes due to reduced water

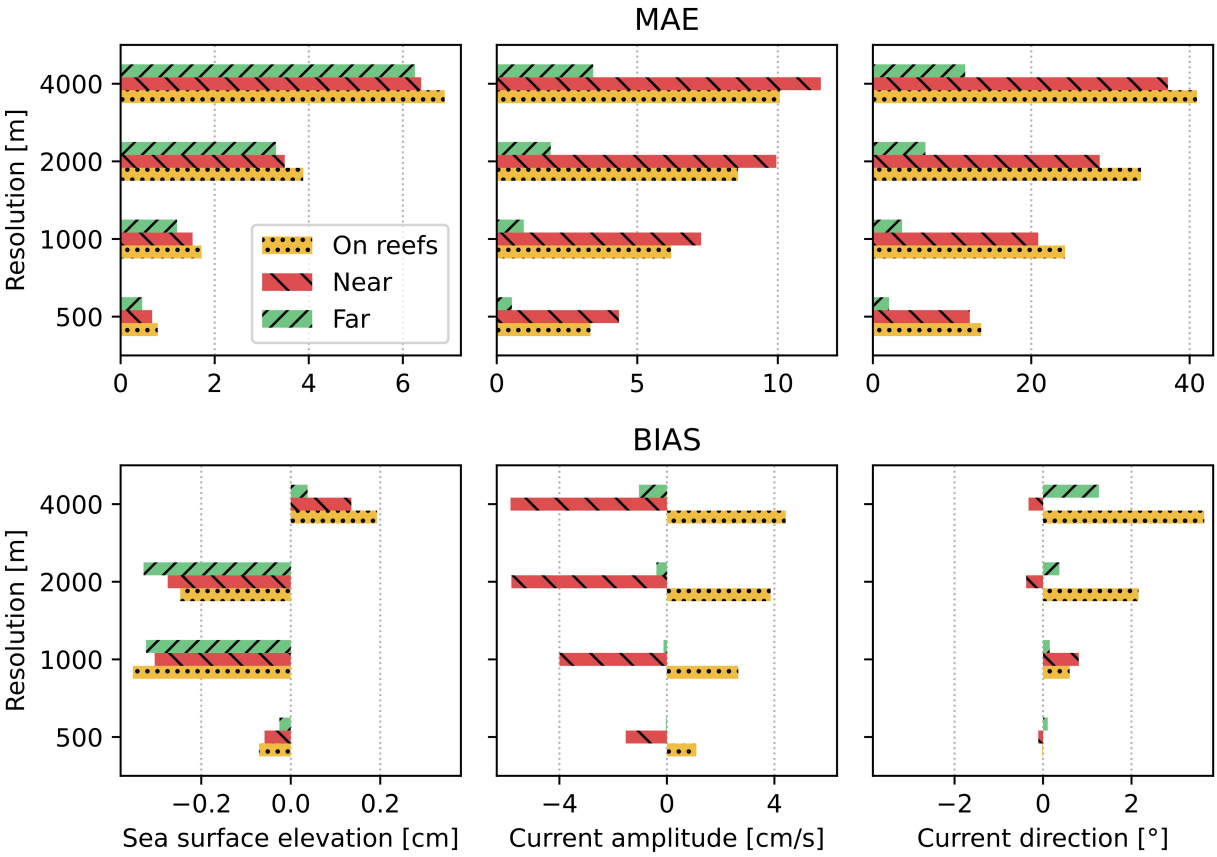

Figure 5: MAE (top) and bias (bottom) of see surface elevation, current amplitude and current direction between the four coarsest resolution setups, computed against the finest 250 m setup. For the three variables, errors increase as the resolution gets coarser. The separation between on reef (yellow), near reef (red) and open-sea (green) points highlights greater differences in current amplitude and direction in the proximity of reefs.

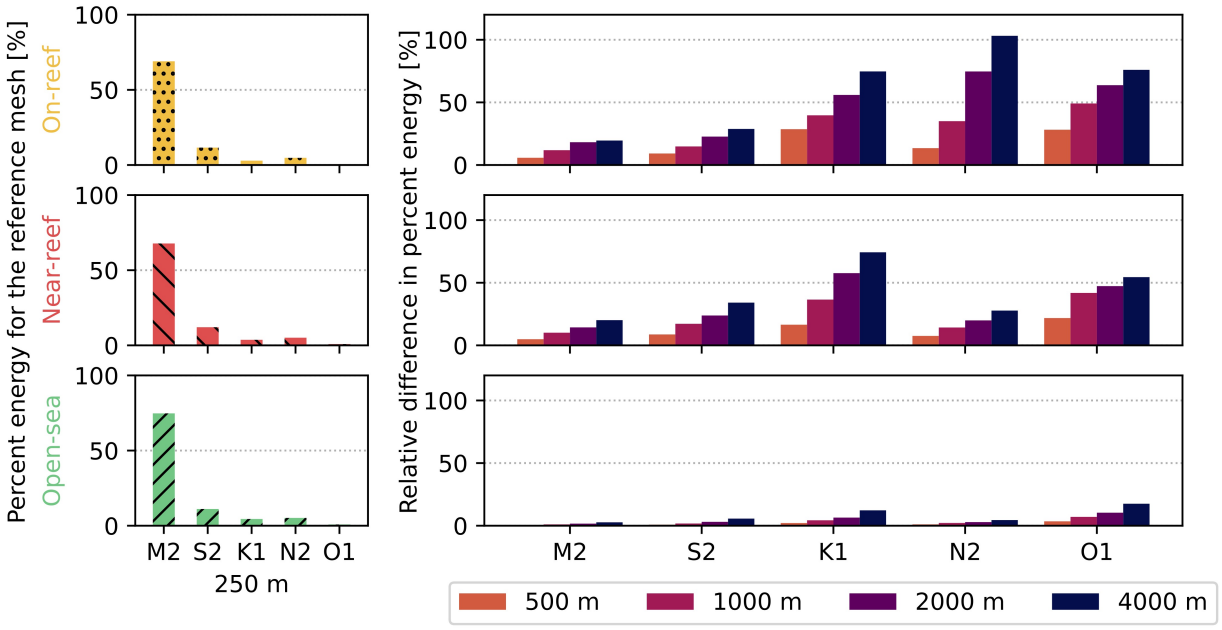

Figure 6: Left: average percent energy of the main tidal constituents for both on reef, near reef and open-sea points as they are computed by the Utide package on the velocities simulated on the finest mesh. This percent energy represents the relative importance of each constituent, which appear to be roughly the same for the two groups of points. Right: Relative differences in percent energy between the finest 250 m setup (used as a reference) and each other setup.

velocity and small-scale recirculation eddies. On coarser meshes, they are be more rapidly flushed away by the faster currents over the reefs. This suggests that achieving high mesh resolution is particularly critical to accurately simulate the local retention of coral or fish larvae at their natal reef.

Finally, the comparison of simulation outputs against field data does not provide insights about model setups' relative quality. Indeed, by computing the MAE between the simulated and observed sea surface elevation, current amplitude and direction at the mooring stations (Fig. 8), it appears that differences between the five mesh setups is much smaller than the difference with the observations. It is noteworthy that none of those stations are located close to the reefs, with distances to the nearest reef varying between 3 km for PPS to 42 km for CCH. The resolution of the five meshes at the mooring stations are hence quite similar, and we therefore cannot expect large differences in simulated currents. In any case, comparing simulated currents with measured ones should be done cautiously: mooring station velocities are given at several depth levels, and were averaged to compare with the barotropic model outputs. As the model bathymetry at the mooring station was linearly interpolated on a rather coarse resolution mesh, there might be non-negligible differences with the real bathymetry, which might explain discrepancies in the current velocity. A detailed validation of the fine-resolution model with observations is included in Appendix A.

4. Discussion and conclusions

Hydrodynamic model simulations are sensitive to the model spatial resolution. This sensitivity is however not spatially uniform and sometimes remains unnoticed. The model resolution has the largest effect where the domain topography or bathymetry are particularly irregular. In coral reef environments, this is typically the case along the coastline, over the reefs and on the shelf break. The sensitivity to the model resolution is much weaker in the open ocean. When validating model outputs with respect to observations, it is important to consider where these observations were collected. If they are collected in the open ocean where the circulation patterns are quite smooth, they will probably yield similar validation results for all model

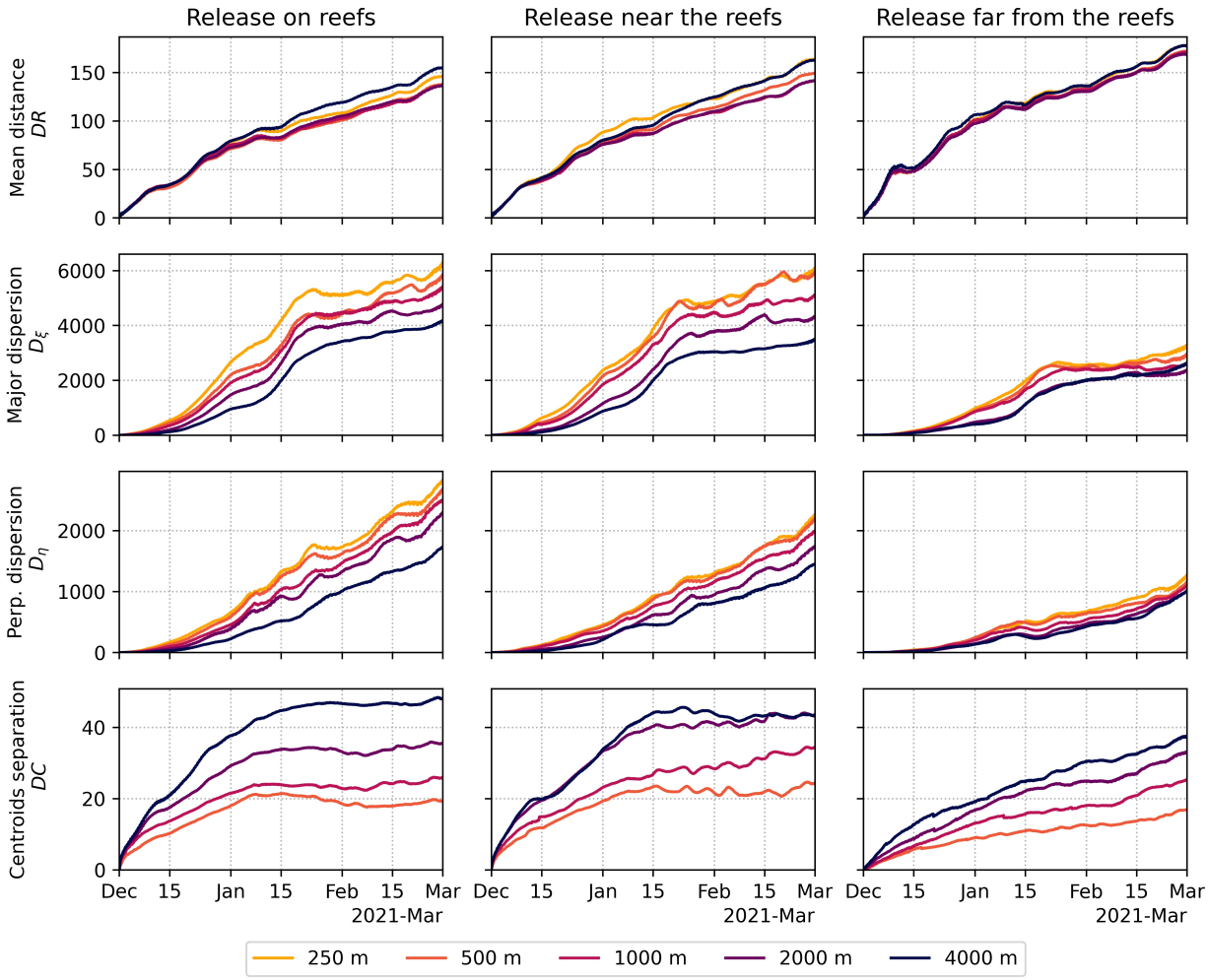

Figure 7: From top to bottom: mean distance between the particle clouds and their release point; average dispersion of the particle clouds in the major and perpendicular directions; and mean separation distance between the particle cloud centroids on the reference 250 m mesh and any other mesh, respectively for particles released from points located on reefs (left), less than 1 km away from reefs (centre) and more than 5 km away from reefs (right).

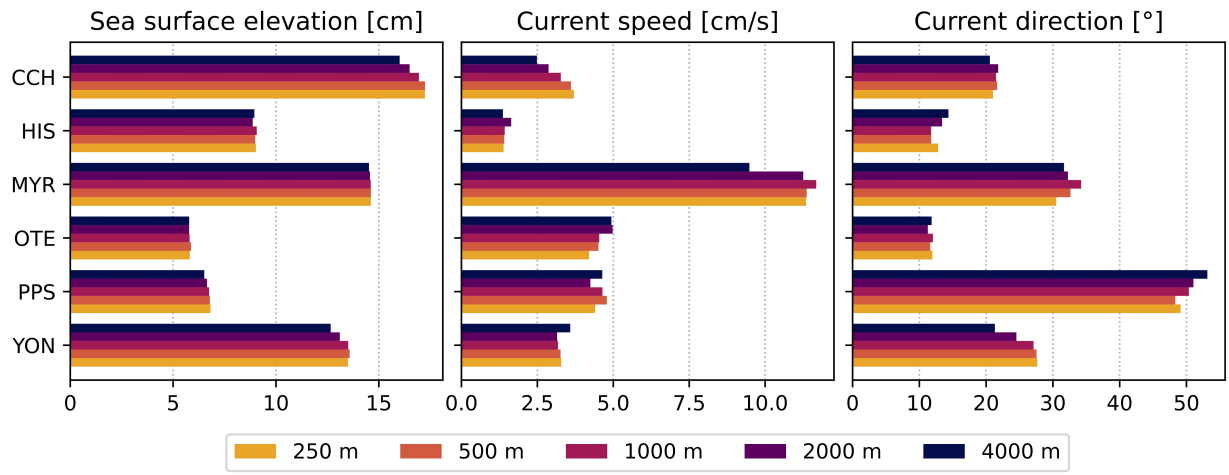

Figure 8: MAE on the sea surface elevation, the current amplitude and the current direction for all models compared to measured values at the five mooring stations, denoted by their usual IMOS code.

resolutions. This can give the misleading impression that a coarse resolution model is appropriate in the entire region, while it is actually only appropriate far away from the coastline and from the reefs. Finally, the impact of the hydrodynamic model resolution is particularly critical when studying transport processes. In that case, discrepancies in the simulated velocity fields have a cumulative effect that can yield large differences over the duration of the transport simulation and hence lead to wrong conclusions.

The first impact of the model spatial resolution is the accuracy with which it will represent the geometry of the area of interest. The coastline topography and seafloor bathymetry are often very irregular and show variations over a broad range of scales. Their small-scales variations will impact the ocean circulation by producing shear, generating recirculation eddies and unevenly dissipating energy. When using a coarse resolution model, the geometry is artificially smoothed and some important geometrical features can be strongly modified. This is for instance the case for separate coral reefs that could be merged together or islands that could vanish or be merged with the mainland (Fig. 3). Here we have shown how a 4 km resolution, which is standard for coastal applications, completely smooths the bathymetry within the GBR dense reef system. It is no longer possible to distinguish individual reefs with such a resolution as their scale is often smaller than the model resolution.

Smoothing the domain geometry in coarse resolution models directly impacts the simulated hydrodynamics. It will be most apparent in topographically complex environments such as near coral reefs and along a rugged coastline. The velocity field is generally more affected than the sea surface elevation. While velocity differences for a fine (250 m) and coarse (4 km) resolution models appear throughout the GBR, they are most apparent near the reefs where they are two to three times larger. This is due to the model representation of the reef's increased rugosity. When the model resolution is coarser than the reef scale, this increased rugosity is spread over an area larger than the reef. Hence, it tends to be too small over the reef and too large in the vicinity of the reef. This leads to an overestimation of the current speed over reefs and an underestimation around them. In other words, the flow tends to be much more uniform within a reef system in a coarse resolution model. When the resolution is fine enough, the flow is then clearly deflected by the reefs. Currents are more intense in the narrow channels between reefs and weaker over the reef canopy. As already discussed by Haza et al. (2012), Zhong and Bracco (2013), and Bracco et al. (2016), a better representation of the topography hence translates into the development of sub-mesoscale features like tidal jets and small-scale eddies, particularly in the wake of reefs.

For many applications, coastal models provide a velocity field that is in turn used to simulate the transport of tracers such as sediments, pollutants, plastics or biological material. In that case, the hydrodynamic model resolution plays an even larger role as the accuracy of the velocity field will have a cumulative effect

on the accuracy of the transport model (Huret et al., 2007; Putman and He, 2013; Dauhajre et al., 2019). In the open ocean, a coarse resolution model will probably provide a satisfactory velocity field for large-scale transport studies (Hoch et al., 2020). However, when the tracer is released near the coast (e.g., sediments from dredging activities) or over the reefs (e.g., coral larvae), the hydrodynamic model resolution will impact the initial tracer dispersal pathways and hence the large-scale plume dynamics. Within a reef system, a fine resolution model will be able to explicitly represent the interactions of the tracer plume with the different reefs. The plume will tend to disperse more (as the flow is more heterogeneous with a fine resolution model) and hence spread over a larger area. Conversely, the more intense eddy dynamics achieved with a fine resolution model will also tend to temporally retain some tracer particles near their release location, and therefore better represent the so-called "sticky waters" effect (Wolanski and Spagnol, 2000; Andutta et al., 2012), as well as the local retention of larvae at their natal reef. This results in a plume that also spreads more "in time", i.e., some tracer particles will take longer to leave the reef matrix than others. All this leads to more dispersive transport patterns when using fine resolution models as opposed to a more advective dynamics when the resolution is coarser. The apparent increase in diffusivity is obviously due to the explicit representation of small-scale processes. Those processes have to be parametrized in coarser resolution models with subgrid-scale models such as the one of Okubo (Okubo, 1971). They will however never be able to fully reproduce the effect of geometrical intricacies on the tracer dynamics. As we have shown, the dispersion within the coral reef system is highly anisotropic. This is probably not specific to the GBR. With coarse models, sub-scale dispersion processes can not be explicitly captured and must therefore be parametrized. We hence underline the importance of assessing the presence and direction of anisotropic transport: if necessary, an anisotropic diffusion tensor should be implemented accordingly.

One important message of our study is that validation is necessary to ensure that the model is behaving correctly, but it is not sufficient to ensure that the model is accurate in all the area of interest. Oceanographic data are often collected in rather deep areas, away from the coast or from reefs. This obviously makes good sense to assess the large-scale circulation patterns. However, to assess smaller-scale topography-driven circulation patterns, one needs to measure flow variables near the coastline or close to reefs. Those environments can present a challenge to deploy and maintain the moorings, and will present more specific flow conditions. In our study, all five model resolutions produced very similar validation results (Fig. 8). Likewise, the performance of Colberg et al. (2020)'s models in terms of current speed, based on the same mooring data, were also similar at resolutions of 500 m and 4 km. This could suggest that a coarse resolution model is sufficient to simulate the hydrodynamics in the GBR. This is however misleading as it only suggests that a coarse resolution model is as effective as a finer one in areas similar to those where the moorings are deployed (i.e., deep open waters). A coarse resolution model that has only been validated in open waters will remain, by design, unsuitable to simulate transport processes in reef environments.

While our study sheds new light on the sensitivity of hydrodynamic models to spatial resolution in complex environments, there are two limitations that will have to be addressed in future works. First, the lack of flow observations in topographically-challenging areas prevents us from validating our models in areas where resolution should matter the most. We have shown that differences between models are the largest near the reefs, but it does not imply that the finest resolution model will be the closest to observations near reefs. However, used at a (very-)high resolution, SLIM has already been shown to accurately simulate small-scale currents in the wake of islands (Delandmeter et al., 2017). Parametrizing the bottom drag of coral reefs remains very challenging (Monismith, 2007; Hoeke et al., 2013; Lentz et al., 2018) as it depends on the reef depth and 3D geometry. In the absence of direct field measurements, we can thus only speculate that a 250 m resolution model is better than one with a 4 km resolution. Our study however suggests that the difference between them is significant.

Another aspect that we did not investigate is the sensitivity to the model physics. Here we only considered a 2D barotropic physics and hence neglected 3D baroclinic effects. While the GBR is generally quite shallow and well-mixed (especially near the coast and near coral reefs), baroclinic processes can still play a role in deeper areas and near river mouths. Overall, we expect the impact of the 3D baroclinic physics to be more limited than the impact of the model resolution since the flow in the GBR is mostly driven by wind and tides (Black et al., 1991; Luick et al., 2007). Testing the model sensitivity to the underlying physics would however allow us to find out whether, for a given computational cost, it would be better to run a

fine-resolution 2D barotropic model or a coarser-resolution 3D baroclinic model.

There is probably no definite answer to the question "how fine is fine enough?". A model resolution should intrinsically depend on the scale of processes of interest. If one is interested in the hydrodynamics of coral reef environments, the model resolution should depend on the scale of the reefs and passages between them. Those are generally of the order of a km or less. We therefore suggest that studies interested in transport processes in coral reef environment (e.g., connectivity studies or sediment pollution impact assessment) should use models with a resolution finer than the reef scale, hence reaching a resolution of at least 250-500 m over the reefs. That range of scales also typically corresponds to the scales at which reef management actions, such as reef restoration and monitoring, or culling of crown-of-thorn starfishes, can be implemented. This is however not the case as coarse resolution models continue to be used to produce reef management recommendations at scales finer than their spatial resolutions. It is therefore important to keep in mind that all models are based on physical and numerical assumptions, and that they can only be used within the scope of validity of those assumptions.

Acknowledgements

We would like to thank Prof. Eric Deleersnijder for the precious advices he gave during the completion of this work.

Computational resources have been provided by the supercomputing facilities of the Université catholique de Louvain (CISM / UCLouvain) and the Consortium des Équipements de Calcul Intensif en Fédération Wallonie Bruxelles (CÉCI) funded by the Fonds de la Recherche Scientifique de Belgique (F.R.S.-FNRS) under convention 2.5020.11 and by the Walloon Region.

Moorings data was sourced from the Integrated Marine Observing System (IMOS) – IMOS is a national collaborative research infrastructure, supported by the Australian Government. The support of the Department of Employment Economic Development and Innovation of the Queensland State Government is also acknowledged. The support of the Tropical Marine Network (University of Sydney, Australian Museum, University of Queensland and James Cook University) on the GBR is also acknowledged.

This research did not receive any specific grant from funding agencies in the public, commercial, or not-for-profit sectors.

References

Andrews, J.C., Bode, L., 1988. The tides of the central Great Barrier Reef. Continental Shelf Research 8, 1057–1085. URL: https://linkinghub.elsevier.com/retrieve/pii/0278434388900398, doi:10.1016/0278-4343(88)90039-8.

Andutta, F.P., Kingsford, M.J., Wolanski, E., 2012. 'Sticky water' enables the retention of larvae in a reef mosaic. Estuarine, Coastal and Shelf Science 101, 54–63. URL: http://www.sciencedirect.com/science/article/pii/S027277141200039X, doi:10.1016/j.ecss.2012.02.013.

Arkema, K.K., Guannel, G., Verutes, G., Wood, S.A., Guerry, A., Ruckelshaus, M., Kareiva, P., Lacayo, M., Silver, J.M., 2013. Coastal habitats shield people and property from sea-level rise and storms. Nature Climate Change 3, 913–918. URL: https://www.nature.com/articles/nclimate1944, doi:10.1038/nclimate1944.

Beaman, R.J., 2010. Marine and Tropical Sciences Research Facility (MTSRF) Project 2.5i.1a Final Report, Reef and Rainforest Research Centre, Cairns, Australia, pp. 13 plus Appendix 1.

Bernhardt, J.R., Leslie, H.M., 2013. Resilience to Climate Change in Coastal Marine Ecosystems. Annual Review of Marine Science 5, 371–392. URL: https://doi.org/10.1146/annurev-marine-121211-172411, doi:10.1146/annurev-marine-121211-172411.

Black, K., Moran, P., Hammond, L., 1991. Numerical models show coral reefs can be self-seeding. Marine Ecology Progress Series 74, 1–11. URL: http://www.int-res.com/articles/meps/74/m074p001.pdf, doi:10.3354/meps074001.

Bracco, A., Choi, J., Joshi, K., Luo, H., McWilliams, J.C., 2016. Submesoscale currents in the northern Gulf of Mexico: Deep phenomena and dispersion over the continental slope. Ocean Modelling 101, 43–58. URL: http://www.sciencedirect.com/science/article/pii/S146350031600038X, doi:10.1016/j.ocemod.2016.03.002.

Bracco, A., Choi, J., Kurian, J., Chang, P., 2018. Vertical and horizontal resolution dependency in the model representation of tracer dispersion along the continental slope in the northern Gulf of Mexico. Ocean Modelling 122, 13–25. URL: http://www.sciencedirect.com/science/article/pii/S1463500317302123, doi:10.1016/j.ocemod.2017.12.008.

Brinkman, R., Wolanski, E., Deleersnijder, E., McAllister, F., Skirving, W., 2002. Oceanic inflow from the Coral Sea into the Great Barrier Reef. Estuarine, Coastal and Shelf Science 54, 655–668. URL: https://www.sciencedirect.com/science/article/pii/S0272771401908509, doi:10.1006/ecss.2001.0850.

Cheung, M.W.M., Hock, K., Skirving, W., Mumby, P.J., 2021. Cumulative bleaching undermines systemic resilience of the Great Barrier Reef. Current Biology 31, 5385–5392.e4. URL: https://www.sciencedirect.com/science/article/pii/S0960982221013464, doi:10.1016/j.cub.2021.09.078.

Codiga, D.L., 2011. Unified Tidal Analysis and Prediction Using the UTide Matlab Functions. Graduate School of Oceanography, University of Rhode Island Narragansett, RI.

Colberg, F., Brassington, G.B., Sandery, P., Sakov, P., Aijaz, S., 2020. High and medium resolution ocean models for the Great Barrier Reef. Ocean Modelling 145, 101507. URL: http://www.sciencedirect.com/science/article/pii/S1463500319300769, doi:10.1016/j.ocemod.2019.101507.

Critchell, K., Grech, A., Schlaefer, J., Andutta, F.P., Lambrechts, J., Wolanski, E., Hamann, M., 2015. Modelling the fate of marine debris along a complex shoreline: Lessons from the Great Barrier Reef. Estuarine, Coastal and Shelf Science 167, 414–426. URL: http://www.sciencedirect.com/science/article/pii/S0272771415301098, doi:10.1016/j.ecss.2015.10.018.

Dauhajre, D.P., McWilliams, J.C., Renault, L., 2019. Nearshore Lagrangian Connectivity: Submesoscale Influence and Resolution Sensitivity. Journal of Geophysical Research: Oceans 124, 5180–5204. URL: https://agupubs.onlinelibrary.wiley.com/doi/abs/10.1029/2019JC014943, doi:10.1029/2019JC014943.

Delandmeter, P., Lambrechts, J., Marmorino, G.O., Legat, V., Wolanski, E., Remacle, J.F., Chen, W., Deleersnijder, E., 2017. Submesoscale tidal eddies in the wake of coral islands and reefs: Satellite data and numerical modelling. Ocean Dynamics 67, 897–913. URL: https://doi.org/10.1007/s10236-017-1066-z, doi:10.1007/s10236-017-1066-z.

Egbert, G.D., Erofeeva, S.Y., 2002. Efficient Inverse Modeling of Barotropic Ocean Tides. Journal of Atmospheric and Oceanic Technology 19, 183–204. URL: https://journals.ametsoc.org/view/journals/atot/19/2/1520-0426_2002_019_0183_eimobo_2_0_co_2.xml, doi:10.1175/1520-0426(2002)019<0183:EIMOBO>2.0.CO;2.

Fisher, R., O'Leary, R.A., Low-Choy, S., Mengersen, K., Knowlton, N., Brainard, R.E., Caley, M.J., 2015. Species Richness on Coral Reefs and the Pursuit of Convergent Global Estimates. Current Biology 25, 500–505. URL: https://linkinghub.elsevier.com/retrieve/pii/S0960982214016236, doi:10.1016/j.cub.2014.12.022.

Fringer, O.B., Dawson, C.N., He, R., Ralston, D.K., Zhang, Y.J., 2019. The future of coastal and estuarine modeling: Findings from a workshop. Ocean Modelling 143, 101458. URL: https://www.sciencedirect.com/science/article/pii/S1463500319301015, doi:10.1016/j.ocemod.2019.101458.

Ganachaud, A., Cravatte, S., Melet, A., Schiller, A., Holbrook, N.J., Sloyan, B.M., Widlansky, M.J., Bowen, M., Verron, J., Wiles, P., Ridgway, K., Sutton, P., Sprintall, J., Steinberg, C., Brassington, G., Cai, W., Davis, R., Gasparin, F., Gourdeau, L., Hasegawa, T., Kessler, W., Maes, C., Takahashi, K., Richards, K.J., Send, U., 2014. The Southwest Pacific Ocean circulation and climate experiment (SPICE). Journal of Geophysical Research: Oceans 119, 7660–7686. URL: https://agupubs.onlinelibrary.wiley.com/doi/abs/10.1002/2013JC009678, doi:10.1002/2013JC009678.

Geuzaine, C., Remacle, J.F., 2009. Gmsh: A 3-D finite element mesh generator with built-in pre- and post-processing facilities. International Journal for Numerical Methods in Engineering 79, 1309–1331. URL: https://onlinelibrary.wiley.com/doi/abs/10.1002/nme.2579, doi:10.1002/nme.2579.

Grech, A., Wolter, J., Coles, R., McKenzie, L., Rasheed, M., Thomas, C., Waycott, M., Hanert, E., 2016. Spatial patterns of seagrass dispersal and settlement. Diversity and Distributions 22, 1150–1162. URL: http://doi.wiley.com/10.1111/ddi.12479, doi:10.1111/ddi.12479.

Green, A.L., Maypa, A.P., Almany, G.R., Rhodes, K.L., Weeks, R., Abesamis, R.A., Gleason, M.G., Mumby, P.J., White, A.T., 2015. Larval dispersal and movement patterns of coral reef fishes, and implications for marine reserve network design. Biological Reviews 90, 1215–1247. URL: https://onlinelibrary.wiley.com/doi/abs/10.1111/brv.12155, doi:10.1111/brv.12155.

Haza, A.C., Özgökmen, T.M., Griffa, A., Garraffo, Z.D., Piterbarg, L., 2012. Parameterization of particle transport at submesoscales in the Gulf Stream region using Lagrangian subgridscale models. Ocean Modelling 42, 31–49. URL: http://www.sciencedirect.com/science/article/pii/S1463500311001818, doi:10.1016/j.ocemod.2011.11.005.

Hoch, K.E., Petersen, M.R., Brus, S.R., Engwirda, D., Roberts, A.F., Rosa, K.L., Wolfram, P.J., 2020. MPAS-Ocean Simulation Quality for Variable-Resolution North American Coastal Meshes. Journal of Advances in Modeling Earth Systems 12, e2019MS001848. URL: https://agupubs.onlinelibrary.wiley.com/doi/abs/10.1029/2019MS001848, doi:10.1029/2019MS001848.

Hock, K., Doropoulos, C., Gorton, R., Condie, S.A., Mumby, P.J., 2019. Split spawning increases robustness of coral larval supply and inter-reef connectivity. Nature Communications 10, 1–10. URL: https://www.nature.com/articles/s41467-019-11367-7, doi:10.1038/s41467-019-11367-7.

Hock, K., Wolff, N.H., Ortiz, J.C., Condie, S.A., Anthony, K.R.N., Blackwell, P.G., Mumby, P.J., 2017. Connectivity and systemic resilience of the Great Barrier Reef. PLOS Biology 15, e2003355. URL: http://dx.plos.org/10.1371/journal.pbio.2003355, doi:10.1371/journal.pbio.2003355.

Hoeke, R.K., Storlazzi, C.D., Ridd, P.V., 2013. Drivers of circulation in a fringing coral reef embayment: A wave-flow coupled numerical modeling study of Hanalei Bay, Hawaii. Continental Shelf Research 58, 79–95. URL: https://linkinghub.elsevier.com/retrieve/pii/S0278434313000654, doi:10.1016/j.csr.2013.03.007.

Hughes, T.P., Barnes, M.L., Bellwood, D.R., Cinner, J.E., Cumming, G.S., Jackson, J.B.C., Kleypas, J., van de Leemput, I.A., Lough, J.M., Morrison, T.H., Palumbi, S.R., van Nes, E.H., Scheffer, M., 2017. Coral reefs in the Anthropocene. Nature 546, 82–90. URL: https://www.nature.com/articles/nature22901, doi:10.1038/nature22901.

Huret, M., Runge, J.A., Chen, C., Cowles, G., Xu, Q., Pringle, J.M., 2007. Dispersal modeling of fish early life stages: Sensitivity with application to Atlantic cod in the western Gulf of Maine. Marine Ecology Progress Series 347, 261–274. URL: https://www.int-res.com/abstracts/meps/v347/p261-274/, doi:10.3354/meps06983.

IMOS, 2018. Australian National Mooring Network (ANMN) Facility - Current velocity time-series. URL: https://portal.aodn.org.au/.

Kessler, W.S., Cravatte, S., 2013. Mean circulation of the Coral Sea. Journal of Geophysical Research: Oceans 118, 6385–6410. URL: http://doi.wiley.com/10.1002/2013JC009117, doi:10.1002/2013JC009117.

Kulp, S.A., Strauss, B.H., 2019. New elevation data triple estimates of global vulnerability to sea-level rise and coastal flooding. Nature Communications 10, 4844. URL: https://www.nature.com/articles/s41467-019-12808-z, doi:10.1038/s41467-019-12808-z.

Kvile, K.Ø., Romagnoni, G., Dagestad, K.F., Langangen, Ø., Kristiansen, T., 2018. Sensitivity of modelled North Sea cod larvae transport to vertical behaviour, ocean model resolution and interannual variation in ocean dynamics. ICES Journal of Marine Science 75, 2413–2424. URL: https://academic.oup.com/icesjms/article/75/7/2413/4975493, doi:10.1093/icesjms/fsy039.

Lambrechts, J., Hanert, E., Deleersnijder, E., Bernard, P.E., Legat, V., Remacle, J.F., Wolanski, E., 2008. A multi-scale model of the hydrodynamics of the whole Great Barrier Reef. Estuarine, Coastal and Shelf Science 79, 143–151. URL: http://linkinghub.elsevier.com/retrieve/pii/S0272771408001364, doi:10.1016/j.ecss.2008.03.016.

Lambrechts, J., Humphrey, C., McKinna, L., Gourge, O., Fabricius, K.E., Mehta, A.J., Lewis, S., Wolanski, E., 2010. Importance of wave-induced bed liquefaction in the fine sediment budget of Cleveland Bay, Great Barrier Reef. Estuarine, Coastal and Shelf Science 89, 154–162. URL: https://www.sciencedirect.com/science/article/pii/S0272771410002295, doi:10.1016/j.ecss.2010.06.009.

Lawrey, E.P., Stewart, M., 2016. Complete Great Barrier Reef (GBR) Reef and Island Feature Boundaries Including Torres Strait (NESP TWQ 3.13, AIMS, TSRA, GBRMPA). Technical Report. Australian Institute of Marine Science (AIMS), Torres Strait Regional Authority (TSRA), Great Barrier Reef Marine Park Authority. eAtlas Repository. URL: https://eatlas.org.au/data/uuid/d2396b2c-68d4-4f4b-aab0-52f7bc4a81f5.

Legrand, S., Deleersnijder, E., Hanert, E., Legat, V., Wolanski, E., 2006. High-resolution, unstructured meshes for hydrodynamic models of the Great Barrier Reef, Australia. Estuarine, Coastal and Shelf Science 68, 36–46. URL: http://linkinghub.elsevier.com/retrieve/pii/S0272771406000400, doi:10.1016/j.ecss.2005.08.017.

Lentz, S.J., Churchill, J.H., Davis, K.A., 2018. Coral Reef Drag Coefficients—Surface Gravity Wave Enhancement. Journal of Physical Oceanography 48, 1555–1566. URL: https://journals.ametsoc.org/view/journals/phoc/48/7/jpo-d-17-0231.1.xml, doi:10.1175/JPO-D-17-0231.1.

Luick, J.L., Mason, L., Hardy, T., Furnas, M.J., 2007. Circulation in the Great Barrier Reef Lagoon using numerical tracers and in situ data. Continental Shelf Research 27, 757–778. URL: https://linkinghub.elsevier.com/retrieve/pii/S0278434306003785, doi:10.1016/j.csr.2006.11.020.

Madec, G., Bourdallé-Badie, R., Chanut, J., Clementi, E., Coward, A., Ethé, C., Iovino, D., Lea, D., Lévy, C., Lovato, T., Martin, N., Masson, S., Mocavero, S., Rousset, C., Storkey, D., Vancoppenolle, M., Müeller, S., Nurser, G., Bell, M., Samson, G., 2019. NEMO Ocean Engine. URL: https://zenodo.org/record/3878122, doi:10.5281/zenodo.3878122.

Monismith, S.G., 2007. Hydrodynamics of Coral Reefs. Annual Review of Fluid Mechanics 39, 37–55. URL: https://www.annualreviews.org/doi/10.1146/annurev.fluid.38.050304.092125, doi:10.1146/annurev.fluid.38.050304.092125.

Mumby, P.J., Mason, R.A.B., Hock, K., 2021. Reconnecting reef recovery in a world of coral bleaching. Limnology and Oceanography: Methods 19, 702–713. URL: https://onlinelibrary.wiley.com/doi/abs/10.1002/lom3.10455, doi:10.1002/lom3.10455.

Okubo, A., 1971. Oceanic diffusion diagrams. Deep Sea Research and Oceanographic Abstracts 18, 789–802. URL: http://www.sciencedirect.com/science/article/pii/0011747171900465, doi:10.1016/0011-7471(71)90046-5.

Petton, S., Pouvreau, S., Dumas, F., 2020. Intensive use of Lagrangian trajectories to quantify coastal area dispersion. Ocean Dynamics URL: http://link.springer.com/10.1007/s10236-019-01343-6, doi:10.1007/s10236-019-01343-6.

Pickard, G.L.G.L., Pickard, G.L.G.L., Science., A.I.o.M., 1977. A Review of the Physical Oceanography of the Great Barrier Reef and Western Coral Sea. Canberra :Australian Government Publishing Service,. URL: https://www.biodiversitylibrary.org/item/123444.

Pringle, W.J., Wirasaet, D., Roberts, K.J., Westerink, J.J., 2021. Global storm tide modeling with ADCIRC v55: Unstructured mesh design and performance. Geoscientific Model Development 14, 1125–1145. URL: https://gmd.copernicus.org/articles/14/1125/2021/, doi:10.5194/gmd-14-1125-2021.

Putman, N.F., He, R., 2013. Tracking the long-distance dispersal of marine organisms: Sensitivity to ocean model resolution. Journal of The Royal Society Interface 10, 20120979. URL: https://royalsocietypublishing.org/doi/full/10.1098/rsif.2012.0979, doi:10.1098/rsif.2012.0979.

Ringler, T., Petersen, M., Higdon, R.L., Jacobsen, D., Jones, P.W., Maltrud, M., 2013. A multi-resolution approach to global ocean modeling. Ocean Modelling 69, 211–232. URL: http://www.sciencedirect.com/science/article/pii/S1463500313000760, doi:10.1016/j.ocemod.2013.04.010.

Rypina, I.I., Kamenkovich, I., Berloff, P., Pratt, L.J., 2012. Eddy-Induced Particle Dispersion in the Near-Surface North Atlantic. Journal of Physical Oceanography 42, 2206–2228. URL: http://journals.ametsoc.org/doi/10.1175/JPO-D-11-0191.1, doi:10.1175/JPO-D-11-0191.1.

Saint-Amand, A., Grech, A., Choukroun, S., Hanert, E., 2022. Quantifying the environmental impact of a major coal mine project on the adjacent Great Barrier Reef ecosystems. Marine Pollution Bulletin 179, 113656. URL: https://www.sciencedirect.com/science/article/pii/S0025326X22003381, doi:10.1016/j.marpolbul.2022.113656.

Schlaefer, J., Carter, A., Choukroun, S., Coles, R., Critchell, K., Lambrechts, J., Rasheed, M., Tol, S., Grech, A., 2022. Marine plant dispersal and connectivity measures differ in their sensitivity to biophysical model parameters. Environmental Modelling & Software 149, 105313. URL: https://www.sciencedirect.com/science/article/pii/S1364815222000196, doi:10.1016/j.envsoft.2022.105313.

Smagorinsky, J., 1963. General circulation experiments with the primitive equations. Monthly Weather Review 91, 99–164. URL: https://journals.ametsoc.org/doi/abs/10.1175/1520-0493(1963)091%3C0099:GCEWTP%3E2.3.CO;2, doi:10.

1175/1520-0493(1963)091<0099:GCEWTP>2.3.CO;2.
Smith, S.D., Banke, E.G., 1975. Variation of the sea surface drag coefficient with wind speed. Quarterly Journal of the Royal Meteorological Society 101, 665–673. URL: https://rmets.onlinelibrary.wiley.com/doi/abs/10.1002/qj.49710142920, doi:10.1002/qj.49710142920.
Spalding, M.D., Grenfell, A.M., 1997. New estimates of global and regional coral reef areas. Coral Reefs 16, 225–230. URL: https://doi.org/10.1007/s003380050078, doi:10.1007/s003380050078.
Thomas, C.J., 2015. Modelling Marine Connectivity in the Great Barrier Reef and Exploring Its Ecological Implications. Ph.D. thesis. Université catholique de Louvain, Belgium. URL: http://hdl.handle.net/2078.1/166499.
Thomas, C.J., Bridge, T.C., Figueiredo, J., Deleersnijder, E., Hanert, E., 2015. Connectivity between submerged and near-sea-surface coral reefs: Can submerged reef populations act as refuges? Diversity and Distributions 21, 1254–1266. URL: http://doi.wiley.com/10.1111/ddi.12360, doi:10.1111/ddi.12360.
Thomas, C.J., Lambrechts, J., Wolanski, E., Traag, V.A., Blondel, V.D., Deleersnijder, E., Hanert, E., 2014. Numerical modelling and graph theory tools to study ecological connectivity in the Great Barrier Reef. Ecological Modelling 272, 160–174. URL: http://linkinghub.elsevier.com/retrieve/pii/S030438001300464X, doi:10.1016/j.ecolmodel.2013.10.002.
Underwood, J.N., Smith, L.D., van Oppen, M.J.H., Gilmour, J.P., 2009. Ecologically relevant dispersal of corals on isolated reefs: Implications for managing resilience. Ecological Applications 19, 18–29. URL: https://onlinelibrary.wiley.com/doi/abs/10.1890/07-1461.1, doi:10.1890/07-1461.1.
Wolanski, E., 1983. Tides on the Northern Great Barrier Reef Continental Shelf. Journal of Geophysical Research 88, 5953. URL: http://doi.wiley.com/10.1029/JC088iC10p05953, doi:10.1029/JC088iC10p05953.
Wolanski, E., Brinkman, R., Spagnol, S., McAllister, F., Steinberg, C., Skirving, W., Deleersnijder, E., 2003. Chapter 15 Merging scales in models of water circulation: Perspectives from the great barrier reef, in: Elsevier Oceanography Series. Elsevier. volume 67, pp. 411–429. URL: https://linkinghub.elsevier.com/retrieve/pii/S0422989403801320, doi:10.1016/S0422-9894(03)80132-0.
Wolanski, E., Pickard, G.L., 1985. Long-term observations of currents on the central Great Barrier Reef continental shelf. Coral Reefs 4, 47–57. URL: http://link.springer.com/10.1007/BF00302205, doi:10.1007/BF00302205.
Wolanski, E., Spagnol, S., 2000. Sticky Waters in the Great Barrier Reef. Estuarine, Coastal and Shelf Science 50, 27–32. URL: https://linkinghub.elsevier.com/retrieve/pii/S0272771499905280, doi:10.1006/ecss.1999.0528.
Zhong, Y., Bracco, A., 2013. Submesoscale impacts on horizontal and vertical transport in the Gulf of Mexico. Journal of Geophysical Research: Oceans 118, 5651–5668. URL: https://agupubs.onlinelibrary.wiley.com/doi/abs/10.1002/jgrc.20402, doi:10.1002/jgrc.20402.

Appendix A. Hydrodynamic model validation

SLIM outputs are compared to field measurements from the six IMOS mooring stations for which data was available for the simulated period. The location of those moorings stations are highlighted on Fig. 1. The observed sea surface elevation signal is correctly represented at all 6 mooring stations, particularly at stations HIS and OTE in the southern GBR, and at PPS in the central part of the GBR (Fig. A.1 and A.2). Those stations display a mean absolute error (MAE) of less than 9 cm on all meshes for the hourly sea surface elevation. Generally speaking, distributions of simulated daily current direction and amplitude seem to also match the measurements (Fig. A.3 and A.4), with MAE of less than 5 cm/s for the current velocities and around 20° for the current direction. Two notable exceptions appear however: on the one hand, at MYR mooring, SLIM underestimates the current velocity whatever the mesh resolution. Likewise, the comparisons between observed and simulated current direction at PPS display MAEs of 50°. This is probably due to the location of those mooring stations close to the shelf break, thus in areas difficult to capture with a 2D model.

When comparing field measurements with our five simulations, the validations appear to be very similar on all meshes. As those mooring stations are all located at least a few km from any reef, discrepancies between mesh resolutions are not expected.

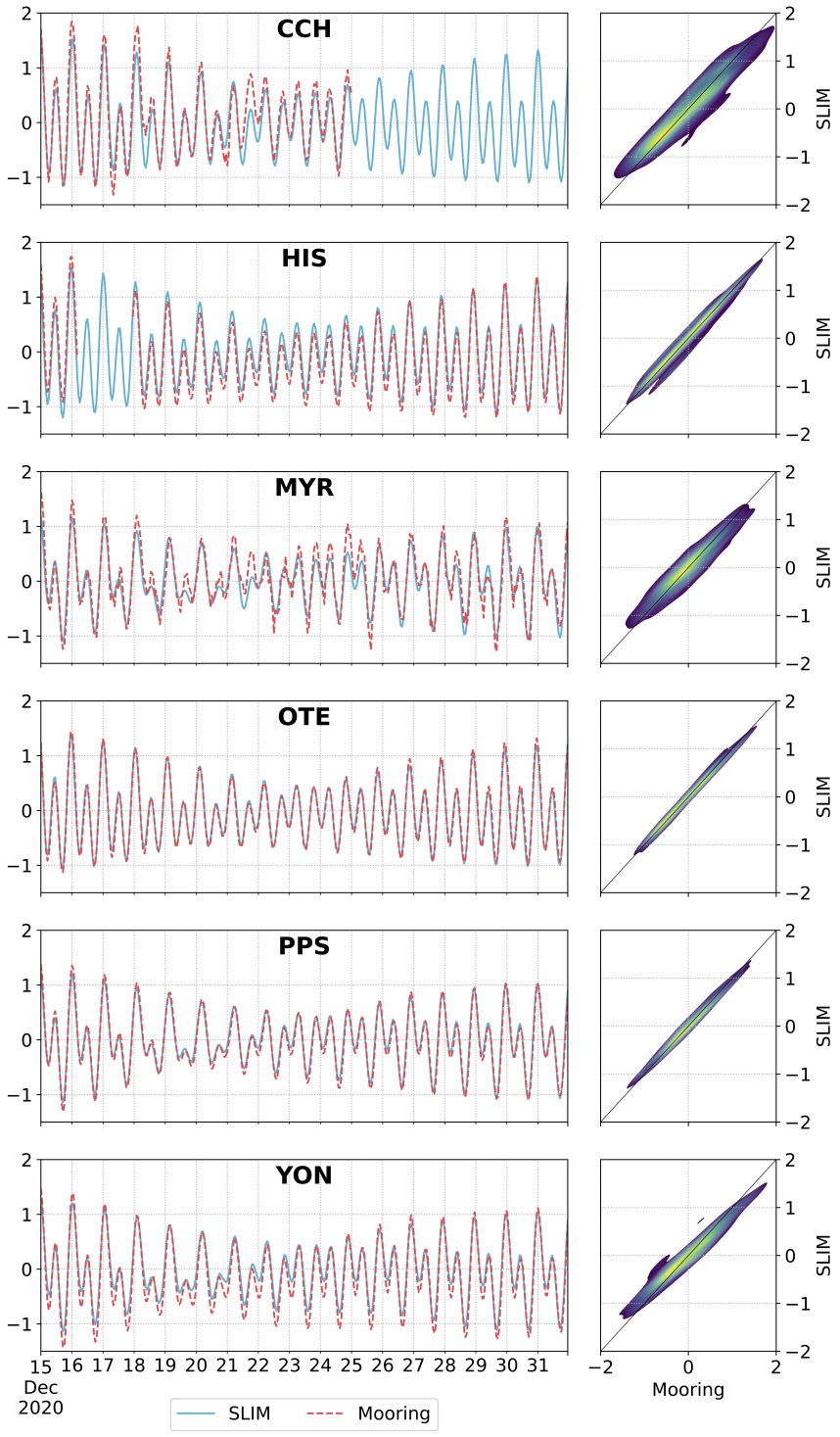

Figure A.1: Comparison sea surface anomalies as observed at the mooring stations and as simulated by SLIM on the 250 m resolution mesh. Left: Subsets of the observed and simulated sea surface anomalies [m] time series between December 15, 2020 and January 1, 2021. Right: Density plots of hourly observed and simulated sea surface anomalies [m] for the entire simulated period.

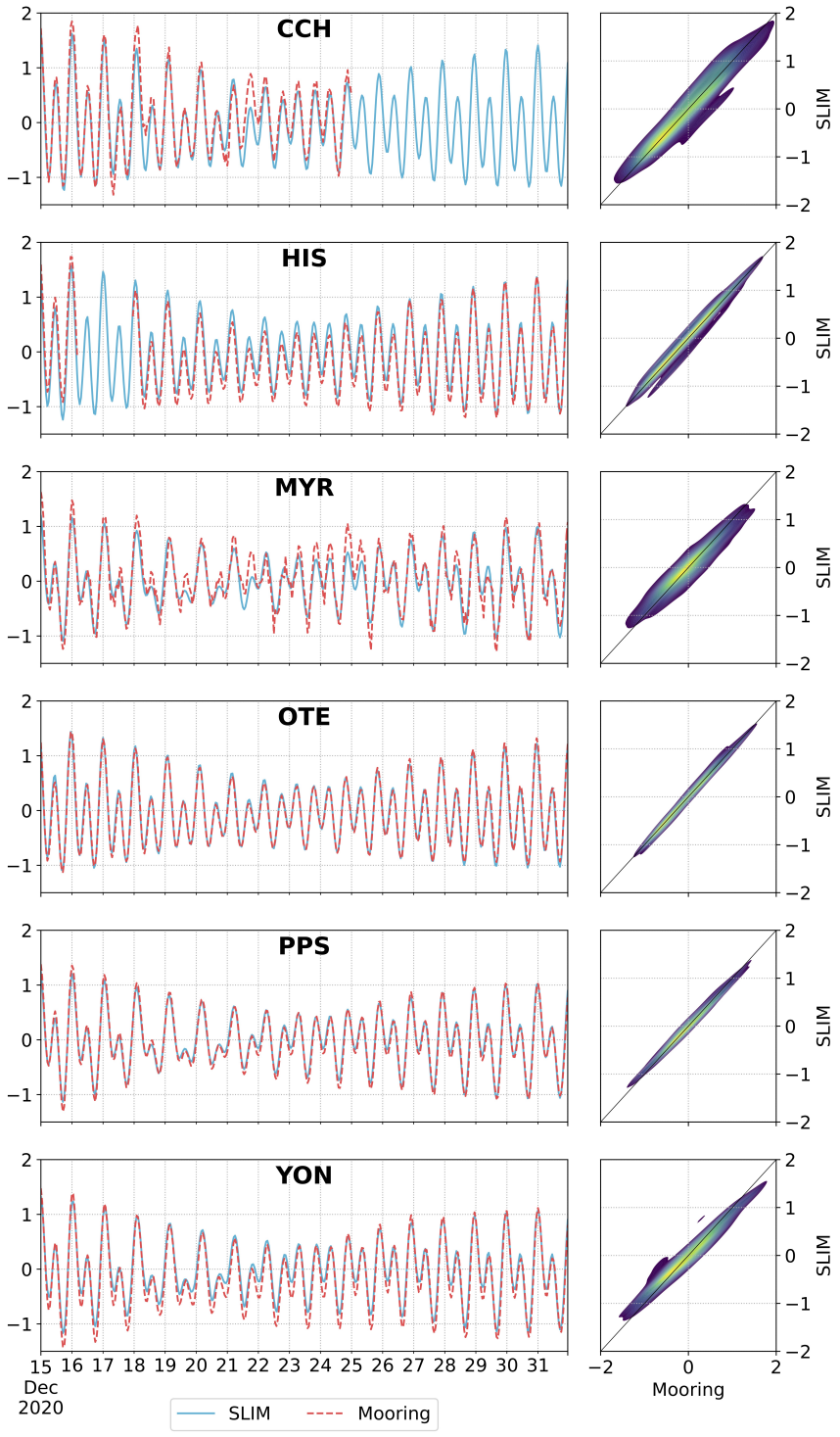

Figure A.2: Comparison sea surface anomalies as observed at the mooring stations and as simulated by SLIM on the 4000 m resolution mesh. Left: Subsets of the observed and simulated sea surface anomalies [m] time series between December 15, 2020 and January 1, 2021. Right: Density plots of hourly observed and simulated sea surface anomalies [m] for the entire simulated period.

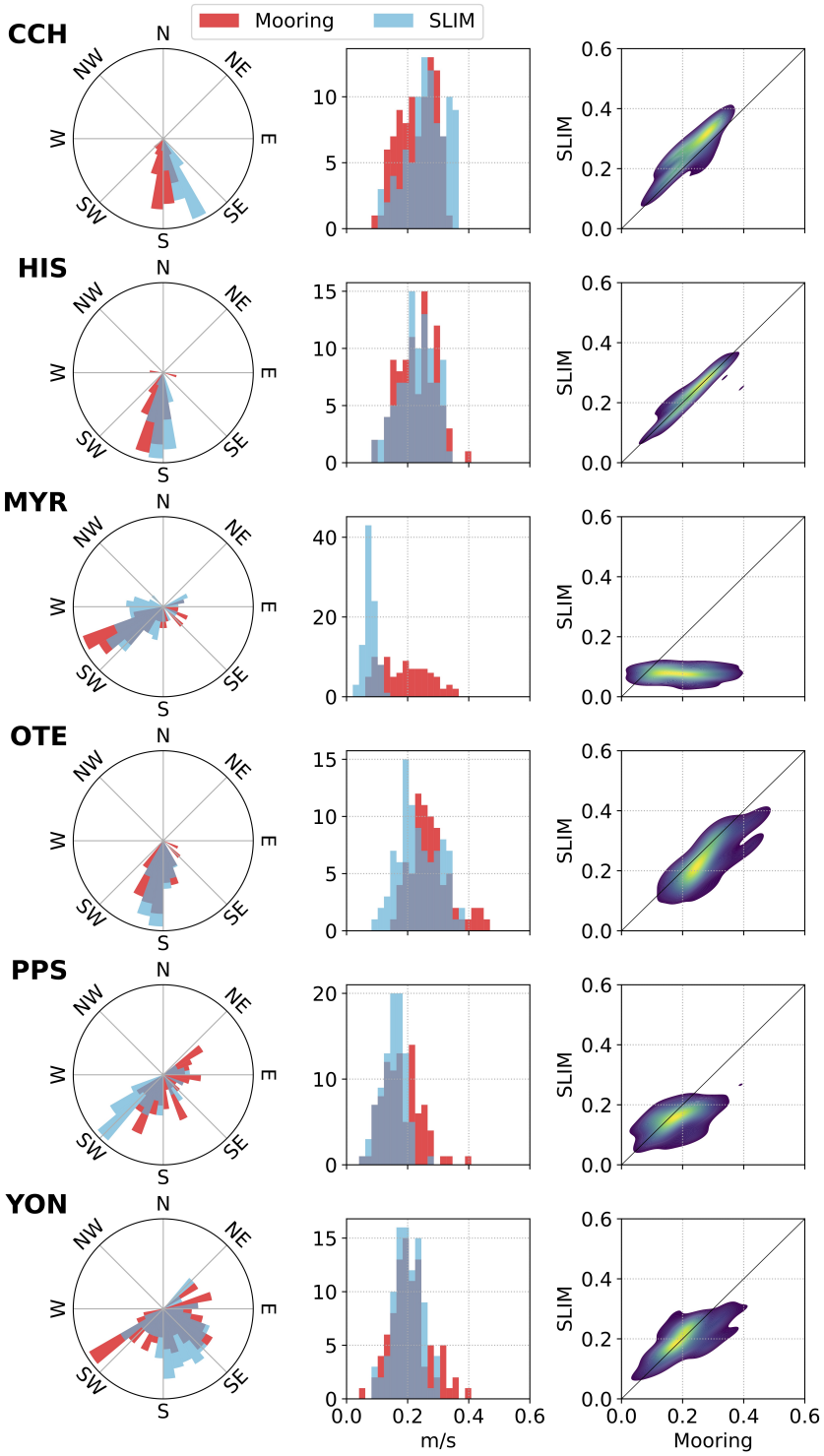

Figure A.3: Comparison of the current direction and velocity as observed at the mooring stations and as simulated by SLIM on the 250 m resolution mesh. Left: histograms of the daily current direction. Center: distribution of the daily current amplitude [m/s]. Right: density plots of the daily observed and simulated current amplitude [m/s].

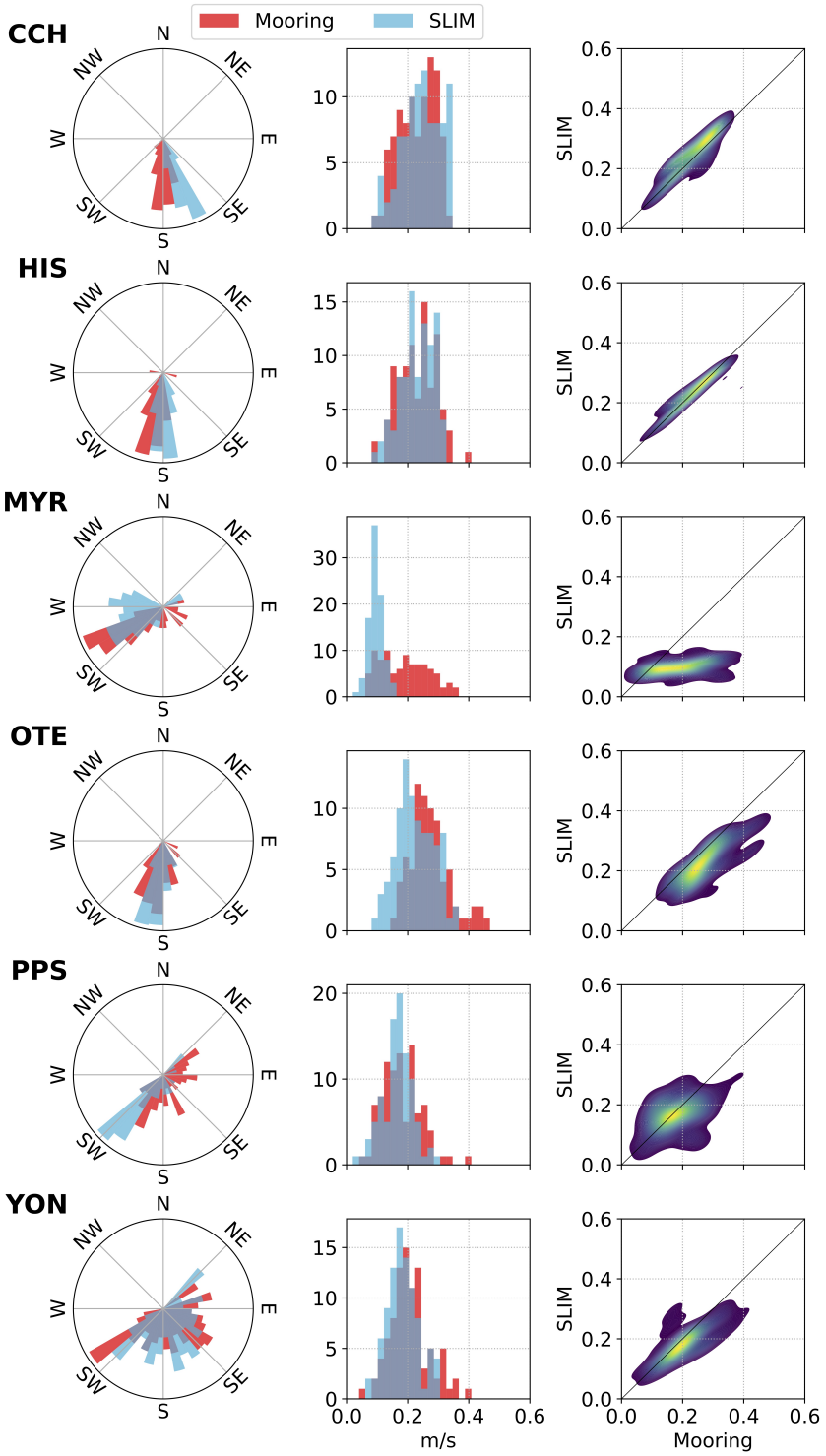

Figure A.4: Comparison of the current direction and velocity as observed at the mooring stations and as simulated by SLIM on the 4000 m resolution mesh. Left: histograms of the daily current direction. Center: distribution of the daily current amplitude [m/s]. Right: density plots of the daily observed and simulated current amplitude [m/s].